chemosensors

MDPI

Review

Chemiresistive Materials for Alcohol Vapor Sensing at Room Temperature

Anna Maria Laera * and Michele Penza

ENEA-Italian National Agency for New Technologies, Energy and Sustainable Economic Development, Laboratory Functional Materials and Technologies for Sustainable Applications, Brindisi Research Centre, Strada Statale 7, Appia, Km. 706, I-72100 Brindisi, Italy; michele.penza@enea.it

* Correspondence: annamaria.laera@enea.it; Tel.: +39-0831-201588

Abstract: The development of efficient sensors able to detect alcoholic compounds has great relevance in many fields including medicine, pharmaceuticals, food and beverages, safety, and security. In addition, the measurements of alcohols in air are significant for environmental protection because volatile alcohols can have harmful effects on human health not only through ingestion, but also through inhalation or skin absorption. The analysis of alcohols in breath is a further expanding area, being employed for disease diagnoses. The analyses performed by using chromatography, mass-spectrometry, nuclear magnetic resonance, ultraviolet-visible spectroscopy, Fourier-transform infrared spectroscopy, or Raman spectroscopy often require complex sampling and procedures. As a consequence, many research groups have focused their efforts on the development of efficient portable sensors to replace conventional methods and bulky equipment. The ability to operate at room temperature is a key factor in designing portable light devices suitable for in situ real-time monitoring. In the present review, we provide a survey of the recent literature on the most efficient chemiresistive materials for alcohol sensing at room temperature. Remarkable gas-sensing performances have mainly been obtained by using metal oxides semiconductors (MOSs), metal organic frameworks (MOFs), 2D materials, and polymers. Among 2D materials, we mainly consider graphene-based materials, graphitic carbon nitride, transition metal chalcogenides, and MXenes. We discuss scientific advances and innovations published in the span of the last five years, focusing on sensing mechanisms.

Keywords: gas sensors; gas sensitive materials; volatile alcohol compounds

Citation: Laera, A.M.; Penza, M. Chemiresistive Materials for Alcohol Vapor Sensing at Room Temperature. *Chemosensors* **2024**, *12*, 78. https://doi.org/10.3390/chemosensors12050078

Received: 12 March 2024
Revised: 2 May 2024
Accepted: 4 May 2024
Published: 7 May 2024

1. Introduction

Volatile alcohols are commonly encountered in both indoor and outdoor environments, being contained in a variety of manufacturing and industrial products such as cosmetics, cleaning products, disinfectants, pharmaceuticals, fuels, and beverages. The measurements of alcoholic compounds are important not only to ensure quality of these products, but also to guarantee safety in workplaces, laboratories, and domestic environments. Volatile alcohols are easily inflammable and harmful for human health. Prolonged exposure to several alcohols can induce visual loss, nasal and mucous inflammation, respiration disorders, neurological disease, and lung irritation [1,2]. Alcohol measurement is also relevant for breath analysis and useful for disease diagnosis. For instance, 1-butanol is considered a biomarker in lung cancer detection and diagnosis. The 1-butanol concentration in breath is significantly higher in lung cancer patients in each stage of tumor development and growth [3,4]. Nowadays, the most widespread breath sensors are designed for ethanol measurement to address breath monitoring and user status checking. Many law enforcement agencies across the globe commonly use portable devices able to quantify ethanol in breath, the technique being less invasive than blood sampling. Widespread methodologies for breath analysis include fuel cells and semiconductor-based

sensors [5]. The routine breath-analysis policy provides an important deterrent to drunken driving, which is responsible for about 50–60% of traffic accidents.

In the last decades, the large variety of applications and requirements described promoted the development of numerous types of alcohol-sensing devices to overcome the problems associated with conventional techniques, such as chromatography, mass-spectrometry, nuclear magnetic resonance, ultraviolet-visible spectroscopy, Fourier-transform infrared spectroscopy, or Raman spectroscopy. These methodologies are not suitable for portability or real-time monitoring and need complex sampling and analysis procedures. The low-cost gas-sensor devices offer a convenient alternative, having simpler structures and operative procedures, a smaller size, lower prices, and lower consumption.

Based on its operating principle, a gas sensor can be classified as electrical, electrochemical, FET-based, capacitive, gravimetric, thermal, optical, or magnetic (Table 1).

Table 1. Operating principle of the main types of gas sensors.

Type of Sensor	Working Principle	Refs.
Electrical	**Changes of resistance, impedance or conductance** in sensitive layer are induced by physical/chemical interaction with analytes molecules (e.g., chemiresistive sensors)	[6–9]
Electrochemical	**Changes of electrical current** in an electrochemical cell are induced by oxidation or reduction of analytes molecules (e.g., amperometric sensors)	[10,11]
FET	**Changes of work function** in a field effect transistor are induced by a charge transfer between the sensing material and the adsorbed analytes molecules (e.g., FET sensors, thin film field effect transistor TFT)	[12–14]
Capacitive	**Changes of dielectric constant of dielectric layer thickness** are induced by physical/chemical interaction with analytes molecules (gas capacitors)	[15]
Gravimetric	**Changes of the vibration resonant frequency** in an electromechanical oscillator are induced by the mass of adsorbed analytes (e.g., surface acoustic wave, micro/nano cantilevers)	[16]
Thermal	**Changes of thermal conductivity** are induced by physical/chemical interaction with analytes molecules (e.g., MEMS)	[17]
Optical	**Changes of optical properties** (absorption, fluorescence, reflection, refractive index, interferometry, optical path length, surface plasmon effects) are induced by physical/chemical interaction with analytes molecules (e.g., Fabry–Perot sensors; absorptive, reflective, and fluorescence-based sensors)	[18–20]
Magnetic	**Changes of magnetic properties** (magnetization, spin orientation) are induced by physical/chemical interaction with analytes molecules (e.g., Hall effect-based magnetic sensors, Kerr effect-based magnetic sensors, magnetostatic surface spin wave oscillator MSSW)	[21]
Memristor	**Change of memristance** in sensitive layer are induced by physical/chemical interaction with analytes molecules (e.g., gasistor)	[22]

Sensor devices also include memristors, an emerging technology, based on resistive-switching phenomena. A memristor is a nonlinear electrical component theoretically described by Leon Chua in 1971 and commonly employed for digital memory applications. The memristors have lower values of baseline resistance with respect to traditional sensors devices relied with metal oxides. In consequence, the memristors allow for improvements of metal oxides-sensing properties at room temperature and the name memristance is also used to indicate the electrical resistance in these devices.

In the present review, we focused attention on materials used in the electrical devices that are the most popular and widespread gas sensors due to their high sensitivity, rapid response and recovery time, excellent stability and repeatability, low cost, ease of use and results interpretation, and facile integration in portable arrays for in situ real time monitoring. The work principle in electrical sensors is based on the changes of resistance, conductance, or impedance upon chemical interaction with gas molecules.

Electrical devices commonly have a tubular geometry or an interdigitated-electrodes geometry that ensures reliability and controllability of the output signals. A tubular gas sensor consists of a ceramic tube coated with the active material and the electrical contacts as shown in Figure 1a. A heater can be placed inside the ceramic tube when high operating

temperatures are required. An interdigital sensor consists of a planar ceramic or polymeric substrate coated with electrodes with finger-like periodic pattern (Figure 1b). The deposition of the sensing material on interdigitated electrodes ensures a remarkably large contact area enabling high sensitivity at room temperature. Flexible polymeric substrates, including polyethylene terephthalate (PET), polyimide (PI), and Kapton, are generally proposed to design wearable interdigital devices [6].

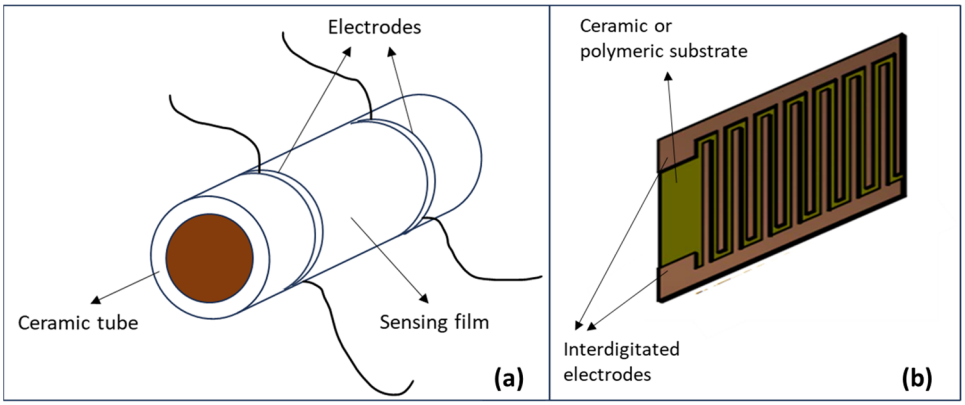

Figure 1. (**a**) Schematic illustration of a tubular gas sensor, and of (**b**) an interdigital gas sensor.

The sensing mechanism generally involves the following three steps: the analytes adsorption, the redox reactions with oxygen ions on surface, and the products desorption.

In the last years, remarkable progress in alcohol sensing at room temperature has mainly been obtained by using metal oxides semiconductors (MOSs), metal organic frameworks (MOFs), 2D materials, and polymers (Figure 2). Among 2D materials, we mainly considered graphene-based materials, graphitic carbon nitride, transition metal chalcogenides, and MXenes.

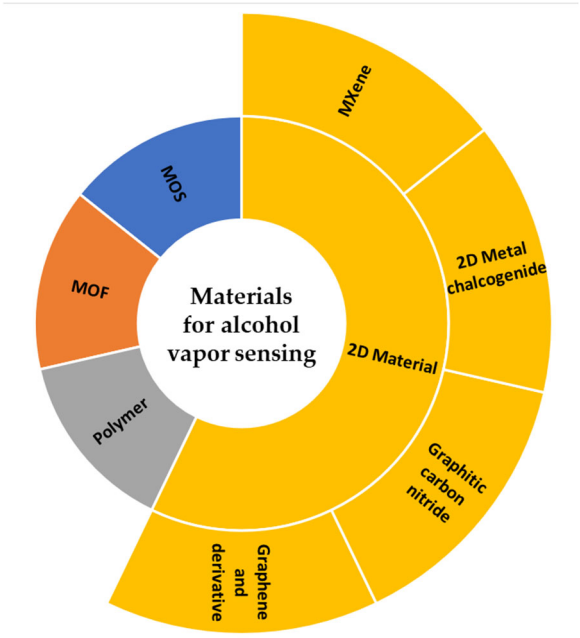

Figure 2. Sensing materials used for detecting alcoholic vapors.

In Sections 2–5 we comprehensively provide a literature review on these sensing materials, pointing out the associated advantages and challenges in terms of sensitivity, response time, and recovery time. For each class of materials, we include evidence regarding the most useful strategies to improve sensing properties at room temperature,

such as doping, defect engineering, introduction of heterojunctions, morphology, and nanostructure design. Significant examples were chosen and described to remark on the potential and efficiency of each strategy. We focused on scientific advances and innovations published in the span of the last five years, in which the research interest for 2D materials-based sensors has reached that previously reserved for the more conventional MOSs-based sensors. While many aspects of the MOSs sensing mechanism have been extensively studied, the sensing mechanism for 2D materials, MOFs, and polymers needs more effort to be clarified. Section 6 describes outstanding examples of memristors designed for gas sensing, named gasistors. Although there are still few gasistors described in the literature, their significant advantageous properties, such as the low power consumption, the simple structure, and the ease of operation characteristics, can inspire new strategies to design innovative gas sensors. Furthermore, Section 7 summarizes the most relevant approaches used to overcome the limits of each class of materials and to improve sensor performance at room temperature. Finally, Section 8 closes the dissertation, outlining the growth prospects of chemiresistive devices.

2. Metal Oxides Semiconductors (MOSs)

The metal oxide semiconductors (MOSs) are probably the most investigated and employed materials in chemiresistive gas sensors because of their outstanding properties including high stability, excellent sensing performances, ease of miniaturization, low-cost synthesis, and manufacturing methods. However, MOSs usually require a high operating temperature in the range of 150–500 °C, accelerating the devices' aging and increasing their power consumption and complexity [23,24].

Several strategies, including doping, tuning defects, and heterojunction formation, have been investigated to improve MOSs sensing performances at room temperature. At the same time, the advancements in synthesis methodologies enabled significant improvement of MOSs sensing properties in forms of nanostructures, such as nanofibers, nanowire, nanorods, and in forms of highly porous structures with exceptional surface/volume ratio. These morphologies facilitate the deep reversible penetration of target gas molecules and, thus, the whole film, and not just the surface, can be involved in gas sensing process.

For instance, Wang et al. showed the good sensitivity toward isopropanol of Bi_2WO_6, obtained in the form of silkworm pupae-like cages assembled with uniformly sized nanorods [25]. The highly porous morphology allowed the detection of isopropanol vapors in the range 10–500 ppm at room temperature. The sensor response, expressed as R_{gas}/R_{air}, where R_{gas} and R_{air} are the resistance of the sensors in alcohol and air, resulted in about 3.8 upon exposure to 500 ppm of isopropyl alcohol. The response and recovery times were determined to be 18 s and 117 s, respectively. Unfortunately, the sensor responses decreased with increasing of relative humidity from 25% to 70%. The proposed sensing mechanism involves the redox reaction between isopropanol and chemisorbed oxygen species. Indeed, under ambient conditions, the MOSs surface adsorbs oxygen molecules able to create a depletion region by trap-ping electrons. The resulting chemisorbed species, such as O_2^-, O^{2-}, and O^-, can react with alcohol molecules. At temperatures below 150 °C, the prevalent oxygen species is O_2^- [26], which can react with isopropanol molecules, as described in following schemes:

$$CH_3CHOHCH_{3(ads)} + 9O_2^-{}_{(ads)} \rightarrow 6CO_2 + 8H_2O + 9e^- \quad (1)$$

The released electrons led to a lower concentration of holes, and, as a consequence, the resistance increase was recorded. The adsorbed oxygen species, able to capture electrons from oxide, were considered responsible for the p-type behavior of Bi_2WO_6. A p-to-n conductivity transition was observed at temperatures higher than 100 °C, with increasing intrinsic electron concentration and decreasing adsorbed oxygen species.

The anodic aluminum oxide (AAO), which is a further example of a highly porous structure, was proposed for ethanol sensing in human breath [27]. The AAO is widely

employed in industry and science research for its controllable nanoscale porosity, biocompatibility, chemical stability, and simple fabrication methods based on aluminum anodization. The suitable choice of fabrication parameters, such as temperature, voltage, and time, allows for finely tuning the pore size and structure. Sensor responses of 2.3%, 8.9%, 14.9%, 23.0%, and 33.6% were recorded upon exposure to 100, 300, 500, 700, and 1000 ppm of ethanol, respectively. In this case, the sensor response was calculated with the formula $(R_{gas} - R_{air}) \times 100/R_{air}$. The authors exploited the linear relationship between response and alcohol concentration for application in human breath testing. The ethanol exhibited better adsorption on the AAO pore walls with respect to water molecules. Upon exposure to ethanol, an increase of electrical resistance was observed due to absorption of alcohol molecules in place of water molecules.

Among MOSs with a high specific surface area, ZnO multifaced nanobristles also showed excellent sensitivity towards ethanol in the concentration range of 50–150 ppm at room temperature [28]. The tested architecture was obtained by thermal decomposition of zinc nitrate at 400 °C. A gas-sensing response (R_{air}/R_{gas}) of 464 was recorded upon exposure to 100 ppm of ethanol.

The high sensing performances at room temperature of 3D hierarchical flower-like TiO_2 microstructures were demonstrated by Wang et al. [29]. TiO_2 was widely tested in gas sensing due to its environmental friendliness, chemical stability, low cost, and wide band gap (3.1 eV) [30]. However, high operating temperatures are usually required. TiO_2 is a n-type semiconductor, but interestingly, the 3D hierarchical flower-like TiO_2 microstructures exhibited a p-type sensing behavior, ascribable to presence of titanium vacancies. A post-synthesis calcination treatment performed at an elevated temperature (500 °C) in air for long time favored the reaction with oxygen molecules, which resulted in a higher concentration of titanium vacancy with respect to the oxygen vacancy. The flower-like TiO_2 microstructures showed high sensitivity upon exposure to different ethanol concentration in the range of 10–500 ppm at room temperature.

Improved sensor performance can be obtained not only by increasing the surface/volume ratio, but also by introducing suitable heterojunctions. For instance, the role of p-n heterojunctions in NiO/SnO_2 nanocomposites was well described by Jayababu et al. [31]. NiO semi-shielded SnO_2 nanoparticles were synthetized by using a co-precipitation technique followed by a sol-gel method. Surface morphological analysis revealed the sample porosity, which enhanced the diffusion and adsorption of vapors. For the NiO/SnO_2 nanocomposite, the sensor response of 140 (R_{air}/R_{gas}) was recorded at around 100 ppm ethanol at room temperature. The resulting response values were about nine times higher than those of SnO_2 sensors and 11 times higher than those of NiO sensors (Figure 3a). Furthermore, the NiO/SnO_2 showed a faster response time (23 s) and recovery time (13 s) with respect to pure oxides components. The superior gas-sensing properties were ascribed to material porosity and, primarily, to the p-n interfaces. The formation of heterojunctions formation the transfer of electrons from the n-SnO_2 to the p-NiO and the transfer of holes from p-NiO to n-SnO_2 until the equalization of the Fermi level. The charges' movements caused the formation of a depletion layer, as shown in Figure 3b. The depletion-layer thickness was reduced as a consequence of the release of electrons in the reaction between ethanol molecules and chemisorbed oxygen species, as described in the following scheme:

$$CH_3CH_2OH_{(ads)} + 3O_2^{-}{}_{(ads)} \rightarrow 2CO_2 + 4H_2O + 3e^{-} \quad (2)$$

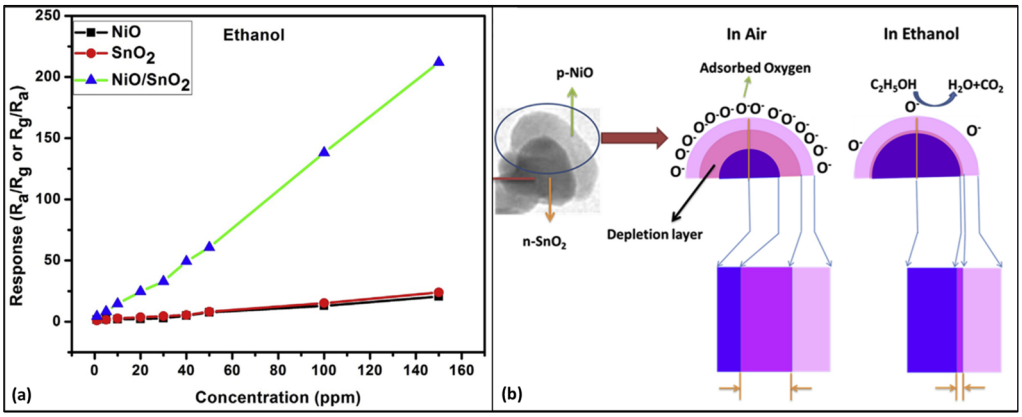

Figure 3. (**a**) Responses of NiO/SnO_2, SnO_2, and NiO sensors upon ethanol exposure at different concentrations at room temperature. (**b**) Schematic illustration of NiO/SnO_2 gas-sensor mechanism. (Reprinted/adapted from [31]).

The modulation of the depletion region at the p-n interface was considered the main factor to sensing-performance enhancement of the NiO/SnO_2-based sensor. The porosity and the high catalytic activity of NiO also contributed to improved sensitivity and a reduction in response and recovery time.

Further examples of heterojunctions, useful for ethanol sensing at room temperature, were described in a ZnO/NiO composite with a nano-worm morphology [32], and in a ZnO/GaN heterostructure fabricated by electrodeposition of flower-like ZnO on GaN substrates [33]. Similarly, a NiO/CeO_2 composite was employed for isopropanol sensing at room temperature [34].

Garcia Osorio et al. enhanced the sensitivity of hematite (α-Fe_2O_3) towards ethanol by incorporation of noble-metal nanoparticles [35]. At the α-Fe_2O_3/Ag heterojunction, electrons moved from silver to hematite, the work function of hematite being higher than the work function of silver. The resulting increase of hematite electron density boosted the chemisorption of oxygen species able to react with ethanol molecules. In addition, the Ag nanoparticles acted as a sensitizer since ethanol can occupy extra active sites on their surface. The best performance in terms of sensitivity, response, and recovery time was obtained with 3.0 wt% of Ag nanoparticles. An excessive loading of silver, closer to 5.0 wt%, drastically decreased the sensor responses because of the larger conductivity and charge recombination. High values of relative humidity also induced a decrease in sensor sensitivity.

An uncommon example of a p–n homojunction was obtained coating n-TiO_2 nanotubes with p-TiO_2 nanoparticles [36]. The vertically aligned TiO_2 nanotubes, having a diameter of 50–70 nm and a wall thickness of 20–22 nm, furnished a 1-D pathway to transport charge carriers between the electrodes. The TiO_2 nanoparticles, having smaller size (<10 nm), partially penetrated the nanotubes, producing a porous structure and forming multiple inner and outer junctions. The homojunction-based sensor showed a maximum response of 57% [$(R_{air} - R_{gas}) \times 100/R_{air}$] upon exposure to 100 ppm of ethanol with fast response and recovery times of 30 and 16 s, respectively.

The combination of hollow nanostructures with doping is an alternative strategy able to increase specific surface area, to facilitate gas diffusion, and to introduce more adsorption/desorption sites for analyte molecules. In this regard, F-doped SnO_2 nanofibers, produced through solution blow spinning, showed high sensitivity towards ethanol with good reproducibility and long-term stability [37]. Solution blow spinning was chosen as it is a cheap and highly scalable technique to produce micro- and nanofibers through coaxial nozzles, through which polymer and hybrid precursor solutions were blown. During the spinning process, solvent concentration decreased more rapidly on the exposed fibers surface because of the rapid evaporation. The resulting concentration gradient along the fiber radius induced solvent diffusion and the Sn^{2+} were dragged from the center to the surface. The large polymer molecules mainly occupied the center of fibers

due to their lower mobility and diffusivity. An annealing treatment at 700 °C was used to remove the polymer and to obtain the mesoporous hollow F-doped SnO_2 nanofibers. The directional morphology facilitated carrier transport while the channels inside the hollow structure enhanced the diffusion of ethanol molecules. Several dopant concentrations were tested, but the best sensing performances were recorded by using the 15 mol% F/SnO_2-based sensor with a maximum sensing response of 5.53 (R_{air}/R_{gas}) for exposure to 100 ppm of ethanol. Analogous undoped SnO_2 nanofibers showed a sensor response 7.4 times lower, being less conductive. The fluorine doping led to more free electrons that facilitated oxygen adsorption through electron trapping at room temperature. The lattice of 15 mol% F/SnO_2 nanofibers was characterized by the smallest crystallite size among all tested compositions. In summary, the excellent sensing performance was ascribed to several factors including the mesoporous hollow structure, the improved conductivity upon F doping, and the presence of numerous nanograin/nanograin junctions on which oxygen molecules were preferentially adsorbed. For application in real-life conditions, the moisture resistance needs to be improved, considering that sensor performance is significantly affected by high values of relative humidity.

The Ce-doping proved beneficial to improving the sensing properties of $LaCoO_3$ upon exposure to high concentration aof ethanol (10–40%) at room temperature [38]. The $LaCoO_3$ is an example of perovskite-type oxide with a crystal structure similar to that of the mineral perovskite ($CaTiO_3$) and a typical formula ABO_3, in which A and B are two different cations [39]. The introduction of Ce^{3+} as dopant decreased the size of nanostructured components of $LaCoO_3$, including short rods and small spheres. In addition, the formation of lattice defects and the presence of CeO_2 was observed in doped $LaCoO_3$. Smaller crystallites with a higher specific surface area and structural defects provided more active sites for the adsorption of ethanol molecules.

A further recent strategy to enhance MOSs sensing performance is based on intrinsic defects engineering [40,41]. The electron density of sensing materials can be incisively tuned by introducing defects, such as oxygen vacancies, that are able to improve either the electrical conductivity or the absorption of target gas molecules. Recently, the introduction of oxygen vacancies in an ultraporous layer of ZnO nanoparticles was proposed to enhance gas-sensing performances toward ethanol [42]. An ultraporous ZnO network, with a thinness of 6 μm, was fabricated by using flame-spray pyrolysis and, afterwards, oxygen vacancies were introduced by deep ultraviolet photoactivation (DUV) at 200 °C (Figure 4a). The ZnO nanoparticles aggregated in large fractal structures with a porosity of about 98%. The presence of large pores of 1–4 μm and small mesopores of a few tens of nanometers was attested to by acquiring SEM images, shown in Figure 4b,c. The exceptional porosity of the produced ZnO enabled the inclusion of oxygen vacancies not only on the surface but also several micrometers below the surface.

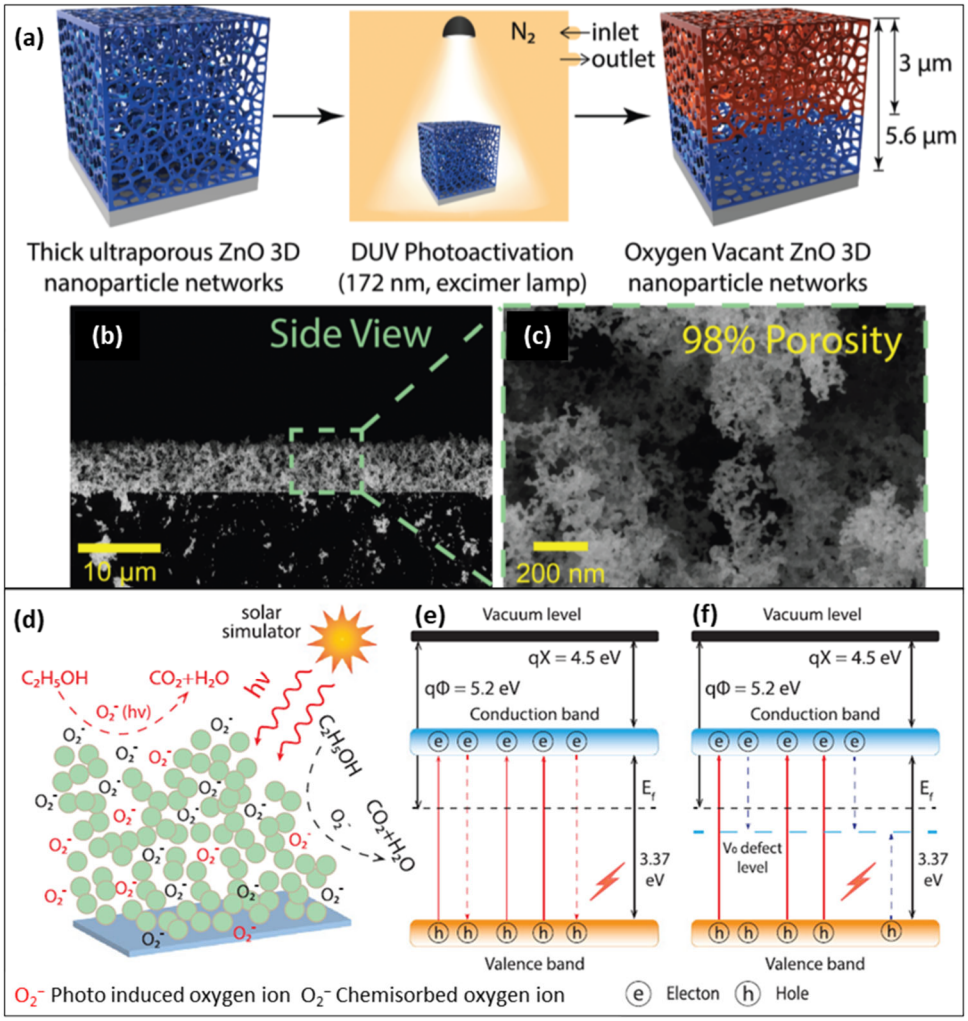

Figure 4. (**a**) Schematic illustration of DUV photoactivation for thin ultraporous ZnO nanostructure; (**b**,**c**) Cross-sectional SEM images of ZnO ultraporous nanostructure at different magnifications; (**d**) Schematic illustration of ethanol-sensing mechanism involving chemisorbed oxygen ions under solar irradiation; (**e**) Energy-band structure of pristine ZnO; (**f**) Energy-band structure of oxygen vacant ZnO (Reprinted/adapted from [42]).

Both prepared and oxygen-vacant ZnO films showed excellent performance as ethanol-sensing materials. The sensor responses were calculated as $I_{gas}/I_{air} - 1$, where I_{gas} and I_{air} were the intensity current of the sensors in ethanol and air. All tests were performed in dry air under solar illumination. The integration of a light-emitter component with low power consumption in gas-sensing microsystems is widely used to enhance room-temperature performances. A schematic illustration of the sensing mechanism involving chemisorbed oxygen ions is provided in Figure 4d. At room temperature, the average sensor response of as-prepared ZnO increased from 0.02 to 4.3, with alcohol concentration increasing from 10 ppb to 1 ppm. It's good sensitivity can be ascribed to the exceptional porosity and specific surface area. The average sensor response of oxygen-vacant ZnO increased from 0.18 to 10.41, with increased alcohol concentration in the same range of 10 ppb–1 ppm. The introduction of oxygen vacancies produced an increase of 83% in the response to 1 ppm of ethanol. The improved sensing performances were ascribed to the synergistic effects of photoinduced ions, unpaired electrons, high concentrations of oxygen vacancies even in deep layers, exceptional porosity, and specific surface area. The average response and recovery time also improved in the presence of oxygen vacancies and reached about 6 min under exposure to 20 ppb of ethanol, while a double time of about 11–12 min was required for as-prepared ZnO. Lower sensor responses were recorded in relative

humidity of 30%, 50%, and 70% due to decrease of reaction sites available to ethanol adsorption in the presence of the interfering water molecules.

The presence of oxygen vacancies lowers the band gap in metal oxides (Figure 4e,f), and, consequently, improves conductivity. Easier electron mobility favors the sensing reactions, and higher sensitivity at room temperature can be reached. Furthermore, oxygen vacancies promote the formation of more chemisorbed oxygen species, providing a large number of sites for reaction with ethanol molecules.

A less investigated strategy to activate MOSs gas sensitivity involves the surface modification with organofunctional molecules able to interact with analytes and to influence the MOSs electrical properties. In this regard, Tomic et al. demonstrated the good sensing properties towards ethanol, under UV-light excitation, of oxygen-deficient WO_{3-x} nanowires modified with (3-aminopropyl) triethoxysilane (APTES) [43]. The sub-stoichiometric WO_{3-x} were grown at 390 °C directly on interdigitated electrodes and the silanization of their surface was performed at 120 °C via chemical vapor deposition using an APTES solution. The possible types of interactions between the WO_{3-x} nanowires' surface and the APTES molecules are schematized in Figure 5. The hydroxyl-terminated surface of nanowires can bond one, two, or three ethoxy groups (Figure 5a–c). The polymerization of adsorbed APTES can also occur with the formation of siloxane bonds, as shown in Figure 5d. In addition, the surface silanization can involve the interaction with amino groups (Figure 5e).

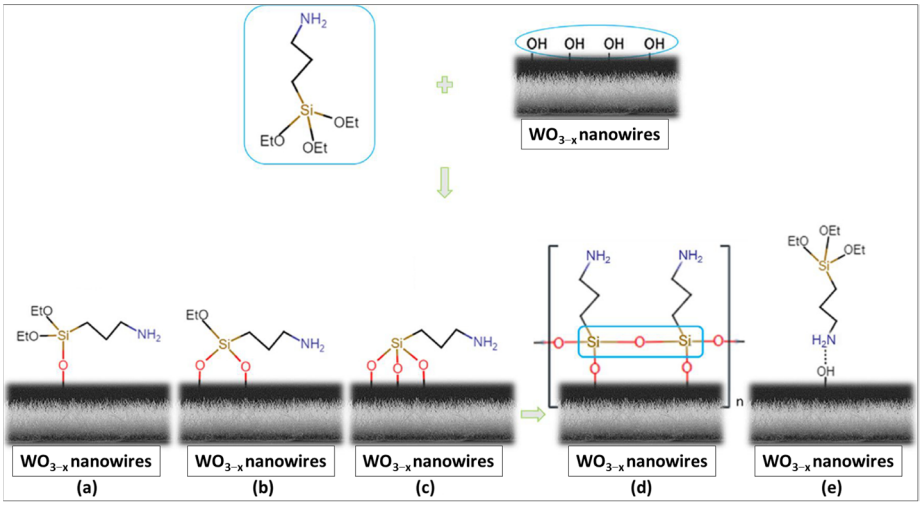

Figure 5. Schematic illustration of the WO_{3-x} surface silanization via oxygen bonding from the (**a**) one, (**b**) two, and (**c**) three ethoxy groups; (**d**) the polymerization of the APTES adsorbed through all three ethoxy groups; (**e**) the interaction with amino group. (Reprinted/adapted from [43]).

For a concentration of 80 ppm of ethanol, the APTES@ WO_{3-x} sensor exhibited a response eight-fold higher with respect to the non-modified WO_{3-x} sensor. The improved sensing performance was ascribed to the presence of amino groups, which facilitated interaction with ethanol vapors, and to the electron transfer between the MOS and the organosilane under UV-light excitation. However, tests performed in humid ambient settings revealed a significant decrease in sensor sensitivity.

3. Metal Organic Frameworks (MOFs)

Metal organic frameworks (MOFs) are a class of nanoporous crystalline materials, produced by the assembly of metal ions or clusters and multidentate organic compounds, that assume the role of linkers in the obtained network [44]. The resulting MOFs structure is robust but flexible due to the presence of relatively weak coordination bonds and intermolecular forces. MOFs are known as the material with the highest surface area, which typically fall within the range from 1000 to 10,000 m^2/g. The pore size can be tuned

by changing the ligand length, while the selective affinity towards analytes can be improved through the functionalization of their inner surface.

Among the MOFs, the subclass of zeolitic imidazolate frameworks (ZIFs) has attracted the attention of researchers for the structures' peculiar structural properties. ZIFs are made of imidazolate likers and metal cations, and have the same topology as inorganic zeolites as well as comparable thermal, architectural, and chemical stability. The charged imidazolate linkers form stronger bonds with metal ions with respect to neutral ligands and, as a consequence, ZIFs preserve crystallinity and porosity when refluxed in water, alkaline solutions, or organic solvents. In the past few decades, hundreds of ZIF structures have been developed for numerous applications including gas sensors [45]. ZIF-8, with the chemical formula $Zn(mim)_2$ (mim = 2-metylimidazolate), is the most extensively studied compound, being commercially available. ZIF-8 displays a sodalite cage that consists of six hexagonal windows and four squared windows, which connect additional cages, as shown in Figure 6 [46].

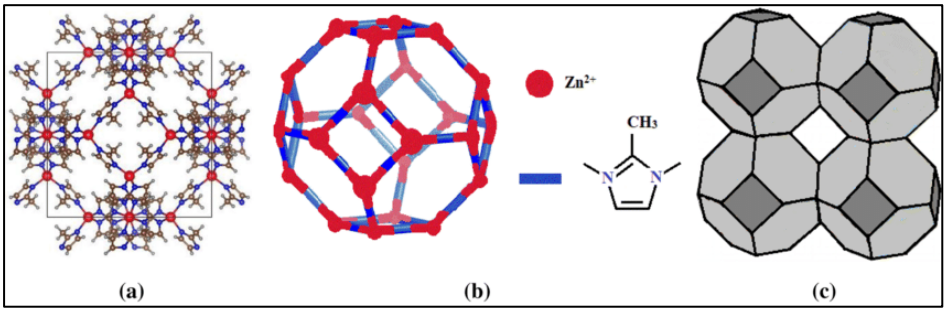

Figure 6. (**a**) ZIF-8 sodalite cage in which Zn, C, N, and H are shown in red, brown, blue, and grey, respectively; (**b**) ZIF-8 ball-and-stick model; (**c**) sodalite topology (Reprinted/adapted from [46]).

The gas diffusion in the ZIF-8 structure is crucially affected by its peculiar flexibility that allows the englobing of molecules larger than the geometric windows. This unexpected adsorption results from torsional motions of imidazole linkers, known as the swing effect [47].

An efficient room-temperature selective methanol sensor was realized by using, as sensing material, a core-shell heterostructure obtained by coating SnS nanoflakes with ZIF-8 [48]. The sensing performances of pure SnS at room temperature are usually unsatisfactory and show low moisture resistance, while the use of pure ZIF-8 results in sensors with an inherent low conductivity. The heterojunction SnS/ZIF-8 allowed for either increasing the ZIF-8 conductivity or improving the sensitivity and selectivity of SnS towards methanol. Furthermore, an excellent stability was observed until 75% of relative humidity and an ultra-low detection limit of 8.27 ppb was calculated. The synthesized heterostructure showed a flower-like architecture able to enhance gas exposure of ZIF-8 nanoparticles, which, in pristine state, appeared highly stacked and agglomerated. The interaction of sulfur lone pairs in SnS with unoccupied orbitals of zinc atoms favored a tight heterojunction formation. The recorded response time and recovery time were 8 s and 30 s, respectively. The noticeable increase in sensor conductivity, following methanol absorption, can be explained considering the reaction with chemisorbed oxygen, as shown below:

$$CH_3OH_{(gas)} \rightarrow CH_3OH_{(ads)} \quad (3)$$

$$2\,CH_3OH_{(ads)} + 3O_2^{-}{}_{(ads)} \rightarrow 2CO_2 + 4H_2O + 3e^{-} \quad (4)$$

The resulting release of electrons leads to an increase of charge carriers in n-type ZIF-8 that can easily reach the SnS/ZIF-8 interface.

ZIF-8 was also used to improve the sensing performance of silicon nanowires (SiNWs) decorated with Ag nanoparticles [49]. The heterojunction formation between SiNWs and ZIF-8 allowed for enhancing the sensitivity to ethanol at room temperature. The SiNWs array was fabricated by a dual metal-assisted chemical etching (dual-MACE),

dipping Si pieces in a solution containing HF and $AgNO_3$. After this first etching, an acid treatment in HNO_3 allowed for obtaining the nanostructured wires. The Ag@SiNWs were produced via reduction of Ag^+ by glucose, which induced the formation of a n-type silicon layer on the surface of p-type SiNWs. Finally, a p-type ZIF-8 was introduced by spin coating of a suitable alcoholic solution. All the major processes involved are schematically reported in Figure 7a.

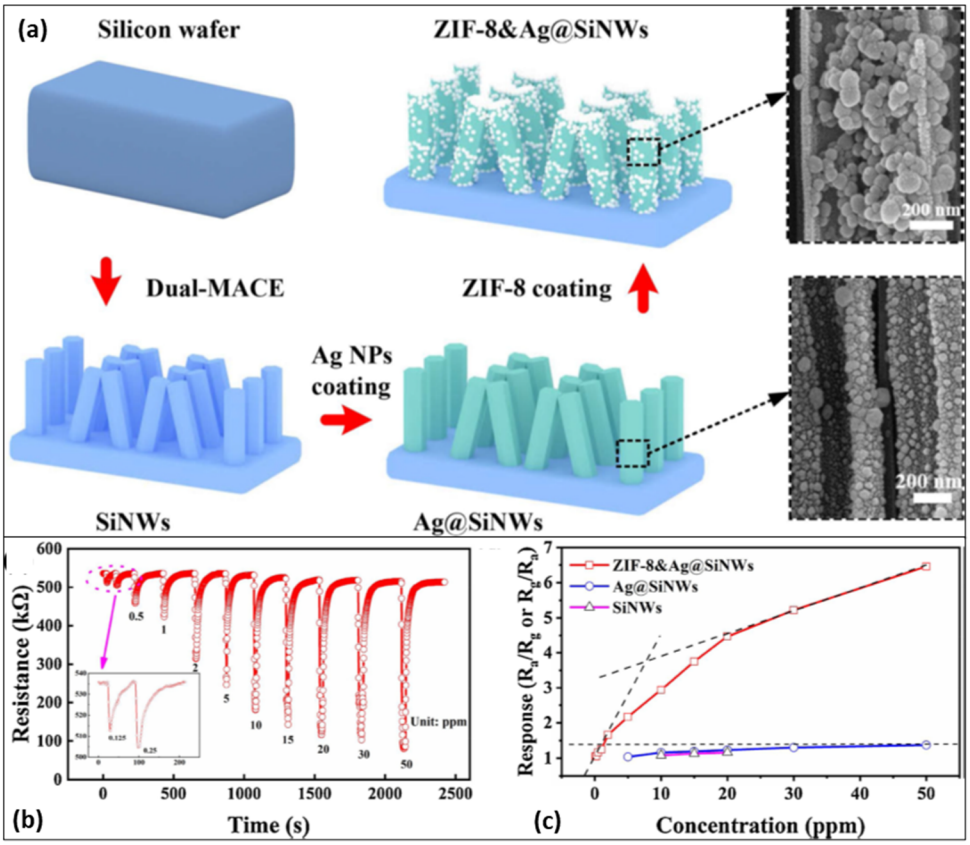

Figure 7. (**a**) Schematic illustration of SiNWs, Ag@SiNWs, and ZIF-8& Ag@SiNWs fabrication; (**b**) Sensor responses of ZIF-8& Ag@SiNWs upon exposure to different ethanol concentrations; (**c**) Response comparison to ethanol for SiNWs, Ag@SiNWs, and ZIF-8& Ag@SiNWs (Reprinted/adapted from [49]).

The resulting ZIF-8& Ag@SiNWs exhibited a remarkably larger variation of electrical resistance upon exposure to ethanol vapors with respect to bare SiNWs and Ag@SiNWs, due to the formation of a heterojunction between the p-type ZIF-8 and n-type superficial layer of silicon (Figure 7b,c). Furthermore, the highly porous structure of ZIF-8 improved ethanol molecules' adsorption and diffusion, favoring a larger charge injection. Significant sensor responses were recorded upon exposure to rarefied ethanol vapor of low to 125 ppb at room temperature and a detection limit of 5.54 ppb was calculated. Rapid response and recovery times of 5.5 s and 45 s, respectively, were measured in the presence of 10 ppm of ethanol. At high humidity values of 85%, significant sensor responses were still recorded. The excellent moisture resistance was explained by considering the hydrophobicity of ZIF-8 nanoparticles, which assumed a barrier role, preventing water molecules from reaching the SiNWs surface. The small amount of H_2O molecules, able to pass through the ZiF-8 layer, was finally adsorbed from Ag nanoparticles that acted as hygroscopic centers. The ZIF-8 also improved the sensor's long-term repeatability and stability, hindering the SiNWs oxidation.

A further promising subclass of MOFs includes two-dimensional conjugated MOFs (2D c-MOFs), a family of conducting materials mainly made from π-conjugated organic

ligands with a planar structure. The peculiar van der Waals layer-stacked arrangement of 2D c-MOFs facilitates high charge-carrier mobility both in-plane and in out-of-plane pathways. In addition to the excellent electrical conductivity, the tailorable band gap and the presence of abundant active sites makes 2D c-MOFs ideal materials for gas-sensing applications [50]. For instance, the phthalocyanine-based $Ni_2[MPc(NH)_8]$ (M = Cu or Ni) was efficiently used to detect methanol at room temperature [51]. Large area $Ni_2[MPc(NH)_8]$ films were produced at a liquid–solid interface on silicon substrate. The wet-interface-assisted liquid–solid method was chosen to finely tune the morphology, thickness, and porosity of deposited films. The surface modification, by grafting octadecyltrimethoxysilane (OTMS), further enhanced the methanol-sensing performance. In particular, the $Ni_2[CuPc(NH)_8]$-OTMS exhibited a significantly faster response and recovery time with respect to pristine sample.

Due to the inherent structure of MOFs, with regularly spaced metal ions and organic linkers, they were also used as suitable precursors to produce homogeneous MOS/C composites with excellent room-temperature sensing performance. For instance, the Cu_3HHTP_2 MOF, made of trigonal 2,3,6,7,10,11-hexahydroxytriphenylene (HHTP) linkers and Cu^{2+} ions, was used to produce a CuO/C hybrid composite through a laser irradiation process [52]. The resulting CuO/C film retained porosity and showed excellent sensing performance towards ethanol over the wide concentration range of 170–3400 ppm. The carbonaceous component consisted of a multilayered graphitic structure formed on the CuO surface. The observed excellent sensing properties were mainly ascribed to the presence of numerous p–p junctions in CuO/C nanoparticles and to the highly porous and homogeneous structure derived from MOF.

Further examples of MOFs-derived porous MOSs are the nano-cubic-structured SnO_2 [53,54] and Fe_2O_3 [55], both obtained through calcination and used to detect butanol efficiently and selectively. These recent publications demonstrated that MOFs can be used as useful templates to synthesize MOSs with outstanding peculiar morphologies, structures, and porosity for sensing applications.

4. 2D Materials

Materials with two-dimensional (2D) morphology have been considered for gas-sensing applications and alcohol detection due to their useful properties such as the large specific surface area, the mechanical robustness, the good environmental stability, the presence of active edges at atomic scale, and the tunable electronic structure. When bulk 2D materials are scaled down to a few layers or until a monolayer, the quantum confinement effects induce the band-gap enlargement and, as a consequence, new tunable electrical and optical properties emerge. Metallic, semimetallic, semiconducting, insulating, or superconducting behavior can be found in 2D materials with different chemical formulas, structural configurations, and surface functionalizations. In each case, the component sheets are held together by van der Waals interactions, which implies minimal interlayer interactions and the confinement of charges inside single monolayers. In a sensing mechanism, both surface adsorption and interlayer swelling can influence the electrical conductivity when gaseous molecules diffuse between the 2D layers of staked structures. Due to their planar geometry and mechanical flexibility, the 2D materials are suitable candidates for the fabrication of wearable devices.

The most relevant 2D materials for gas-sensor design include graphene-based materials, graphitic carbon nitride, transition metal chalcogenides, and MXenes. Each of these four classes of materials presents some drawbacks, which still limits their applications. The zero-gap band of graphene and the instability of metal chalcogenides make difficult the control of gas-sensing performance. Graphene oxide (GO), obtained via graphene oxidation, exhibits high sensitivity but very long recovery times. The graphitic carbon nitride presents low surface area and rapid recombination of electron-hole pairs. The MXenes have high detection limits and poor long-term stability.

The use of composite materials is a common strategy to overcome the limits of individual components and to enhance properties such as sensitivity, selectivity, repeatability, or moisture resistance.

4.1. Graphene and Derivatives Based Gas Sensors

Graphene, the most popular 2D material, is made of sp^2 carbon atoms positioned on the vertices of hexagons. The resulting honeycomb lattice exhibits fast electron mobility, useful to obtain a rapid response toward analytes. The gas-sensing performances of graphene were first investigated by Schedin et al. in 2007 [56]. The extraordinary capability of graphene to detect a single molecule absorbed on its surface was observed thanks to its peculiar electrical behavior with exceptionally low noise values. Schedin's work opened the way to a plethora of publications that demonstrated the efficiency of graphene and derivatives in vapor-detection at room temperature. However, the absence of a gap band in graphene makes it difficult to control the gas-sensing performance. The long recovery time is another relevant limit of graphene-based gas sensors.

Graphene oxide (GO), obtained via graphene oxidation, also exhibits high sensitivity upon exposure to different organic volatile compounds, but with long recovery times. In addition, the content of GO functional groups, such as carboxyl, hydroxyl, and epoxy, is not finely tunable, and an excessive oxidation grade makes GO an insulating material. The described limits can be overcome through physical and chemical modification, including defect engineering, surface functionalization, and elemental doping. The reduction of GO through chemical, thermal, or photo-thermal methods is widely used to produce reduced GO (rGO) with a different carbon-to-oxygen ratio, which determines structural properties, mechanical strength, stability, dispersibility, and gas-sensing properties [57].

Single-layer graphene and GO can be confined into nanometer-wide strips, namely, graphene nanoribbons (GNRs) and graphene oxide nanoribbons (GONRs), which also show attractive sensing performance [58].

The synergistic combination of graphene or GO with other semiconductor materials can greatly enhance sensing capability. Composites of graphene or its derivatives with MOSs show low operating temperature and excellent sensing performance, generally ascribed to a heterojunction formation, a synergetic coupling effect between the two component, and improved morphology and structure [59]. For instance, a SnO_2/rGO composite exhibited good sensing responses at room temperature upon exposure to ethanol in the concentration range of 29–145 ppm [60]. SnO_2 nanoparticles immobilized on graphene sheets were obtained by using a microwave-assisted method. As described for MOSs-based devices, the sensor mechanism relies on the reaction between alcohol molecules and chemisorbed oxygen species. The excellent sensing performance was ascribed to the formation of a n–p heterojunction, between the n-type semiconductor SnO_2 and the p-type rGO, providing better adsorption sites for oxygen adsorption. The electron transfer from rGO to SnO_2 at room temperature was favored for the presence of a low Schottky barrier. The response time and recovery time were determined to be 123 and 128 s, respectively, and a limit of detection of 3 ppm was calculated.

For ethanol sensing, the binary SiO_2/GO composite was also efficiently used [61], and a ternary composite material made of MoO_2-Ni-graphene was proposed by Mehmood et al. [62]. In this last case, by using a hydrothermal process, hierarchical structures of MoO_2 were grown on Ni-graphene thin layers. The Ni and MoO_2 were chosen for their metallic nature, able to enhance oxygen adsorption and ionization. The intrinsic characteristics of the hierarchical structure, with its all-direction open shape and its numerous nanojunctions between adjacent nanosheets, favored the diffusion of analyte molecules. The ternary MoO_2-Ni-graphene composites were annealed in an ambient environment at 300 °C and 400 °C to increase the oxidation level. After thermal treatments, X-ray photoelectron spectroscopy (XPS) was used to confirm the formation of Mo^{6+}, Mo^{5+}, and Mo^{4+} oxidation states. Higher quantities of chemisorbed oxygen species and hydroxyl ion species were also observed. In addition, analysis performed with Raman spectroscopy furnished clear indications about

the increase of defective sites in annealed graphene sheets. Due to the introduction of numerous oxygenated functional groups, the MoO_2–Ni–graphene sensitivity towards ethanol was improved by the elevated annealing temperature. The sample annealed at 400 °C showed the maximum response of 105 (R_{gas}/R_{air}) for 1000 ppm of ethanol with a detection limit of 15 ppm. The hydroxyl groups mainly favored the selective interaction towards ethanol via hydrogen-bonding formation. Good sensing performances were also recorded in the presence of high values of relative humidity.

An alternative ternary composite material, employed for ethanol-sensing at room temperature, was obtained by attaching semispherical Co_3O_4 nanoparticles to both rGO and carbon nanotube (CNTs) surfaces [63]. The resulting Co_3O_4/CNTs@rGO composite exhibited a mesoporous structure with a high surface area of 92.9 m^2/g. The mass ratio of Co_3O_4 loaded on CNTs/rGO was 34%, as calculated with TGA measurements. Upon exposure to 50 ppm of ethanol, a sensor response of 1.36% was calculated with the formula $(R_{gas} - R_{air}) \times 100/R_{air}$.

Graphene and MOFs hybridization was also tested for detection of several volatile organic compounds. Specifically, the graphene hybrid nanocomposite with copper-benzene-1,3,5-tricarboxylate (graphene-Cu BTC) showed high sensitivity toward methanol and chloroform in the concentration range of 2.82–22.6 ppm [64]. The hybrid nanocomposite was produced by using a simple shear mixing method and the sensor device was fabricated through spray deposition onto commercial interdigitated electrodes. Small Cu BTC particles with sizes of 10–15 nm were observed on graphene sheets by using transmission electron microscopy (TEM). Graphene acted as an excellent conductive sensing element while Cu BTC, with large porosity, boosted adsorption capacity. Furthermore, the MOF particles intercalated in the graphene sheets, expanded graphene platelets, and increased defects that operated as additional adsorption sites. The methanol coordination bonds with Cu^{2+} ions also promoted high sensor responses. Graphene hybrid nanocomposites with alternative MOFs, such as zirconium 1,4-dicarboxybenzene and ZIF-8, showed the worst sensing performances.

Other sensor characteristics, including the geometry, shapes, and patterns of the devices, were usually not considered as key features to improve sensor performance. However, the recent work of Hassan et al. demonstrated the different sensing properties of chemoresistive sensors with different fractal geometries [65]. The authors fabricated chemoresistive alcohol sensors through extrusion printing methods by using a graphene-based ink formulated with ethyl cellulose and dihydrolevoglucosenone (Cyrene). Printed 3D structures with a high aspect ratio were obtained on flexible substrates. The encapsulation of graphene flakes within the cellulose-based binder decreased the total sheet electrical resistance. Bare graphene tends to curl up, reducing adhesion between flakes. In the absence of a polymeric binder, a larger sheet resistance can be ascribed to the emergence of electron flow between the tips and the edge of the flakes. The use of ethyl cellulose allowed for reducing sheets' resistance between the flakes and improving the charge transport mobility. An annealing treatment at 250 °C for 30 min further improved conductivity, due to the partial thermal decomposition of ethyl cellulose in aromatic species able to improve stacking between the polymer residues and the graphene flakes. Among the tested structures, the fractal geometry with the higher aspect ratio enhanced sensing performance towards ethanol at room temperature in the concentration range 5–100 ppm. No significant degradation of sensor response was observed in presence of elevate relative humidity. The response and recovery time also resulted improved for the fractal architectures with respect to conventional interdigitate ones. The production of bioinspired fractal geometries using composed graphene ink offers new pathways to design low-cost and environmentally friendly alcohol sensors.

The chemical oxidation of graphene involves the defect formation in the graphene sheets. The possibility to obtain graphene and GO with different concentrations of structural defects was recently exploited to fabricate an electronic nose (EN) able to detect and to distinguish methanol, ethanol, isopropanol, formaldehyde, and acetone at room temperature [66]. An EN englobes a series of sensors whose responses are appropriately

processed to identify the so-called "fingerprint" of the analytes. The proposed EN consisted of two sensors, made with different numbers of graphene layers, and four sensors, made of rGO with different oxidation grades obtained through thermal treatments in the range of 180–250 °C. The experimental setup is schematically reported in Figure 8a. The graphene was produced by exfoliation method using graphite flake as the starting reagent. The electrical contacts in silver of each sensor were inject-printed as interdigitated electrodes on Kapton substrates. Impedance measurements showed faster response and recovery speeds with respect to measurements performed by the application of direct current. The alternating current can accelerate the adsorption/desorption process, improving sensor performance. The rGO-based sensors displayed higher responses than the graphene-based ones, due to the presence of a larger number of defects and oxygenated functional groups able to interact with vapor molecules (Figure 8b). Principle Component Analysis (PCA) was employed for data processing, demonstrating the EN's ability to recognize all the considered organic compound in the concentration range of 10–80 ppm. The arrays showed excellent moisture resistance, the sensor responses being minimally affected until a relative humidity of 90%.

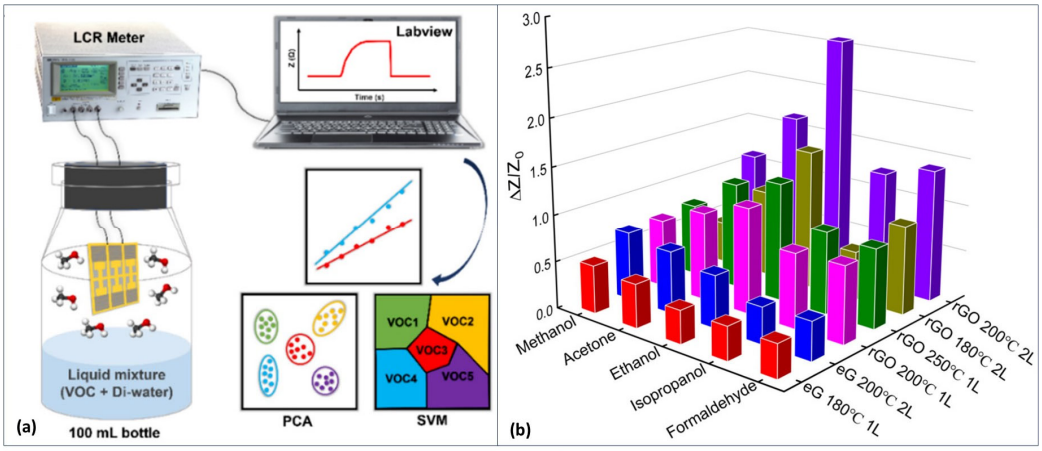

Figure 8. (**a**) Schematic illustration of the impedimetric setups for volatile organic compounds (VOCs) detection; (**b**) Sensor responses from each sensor in the array toward the target VOC at 80 ppm (Reprinted/adapted from [66]).

4.2. Graphitic Carbon Nitride-Based Gas Sensors

The carbon nitride family consists of metal-free organic compounds mainly made of C and N atoms and generally includes triazine and heptazine moieties. The polymeric graphitic carbon nitride (g-C_3N_4), the most stable allotrope of carbon nitrides in ambient atmosphere, was considered as a promising material for gas-sensing due to its advantageous graphitic-like structure and electronical properties [67]. The g-C_3N_4 can be easily synthetized through polymerization of cheap reagents such as melamine, urea, thiourea, cyanamide, and dicyanamide. Ultrathin g-C_3N_4 sheets can be obtained by using exfoliation methods [68] The g-C_3N_4 presents low surface area and rapid recombination of electron-hole pairs, and, consequently, the formation of heterostructure is commonly proposed to improve its sensing performance.

A composite, made of g-C_3N_4 and graphite nanoplatelets (GNPs), was used for ethanol sensing under ambient conditions [69]. The g-C_3N_4 was synthesized by a facile thermal polycondensation method using melamine as the starting reagent. An acid treatment, followed by long-term ultrasonication, allowed g-C_3N_4 chemical exfoliation in nanosheets. The sensing layer was produced by mixing g-C_3N_4 nanosheets with GNPs and carbon paste and using ethyl cellulose as binder. High responses upon exposure to ethanol in the concentration range of 1–10 ppm were recorded at 60% of relative humidity. The further

moisture rise appreciably decreased sensor performance. The porous structure of the active layer favored oxygen's penetration of the nanosheet, improving sensitivity.

The g-C_3N_4 presents a large affinity to oxygen mainly due to pyridine moieties. Also, in this case, the sensing mechanism involves the reactions of alcohol molecules with chemisorbed oxygen species. The released electrons recombine with the holes, i.e., the major charge carriers in p-type g-C_3N_4 composite, leading to resistance increase.

A similar nitrogenated graphene, obtained by pyrolysis of melamine and L-alanine, was used as support for atomically dispersed Zn [70]. In recent years, metal atoms atomically dispersed on solid supports have been extensively employed as catalysts in various reactions, but few studies have been published on gas-sensing performance of these materials [71,72]. Atomically dispersed zinc on nitrogenated graphene was successfully used as a sensing material for ethanol detection at room temperature. Each zinc atom was coordinated by one nitrogen atom and two carbon atoms. A sensor response of 25%, calculated as $(R_{gas} - R_{air}) \times 100/R_{air}$, was obtained upon exposure to 1500 ppm of ethanol with excellent selectivity and stability. The response time and recovery time were 102 s and 550 s, respectively. The detection mechanism, investigated through DFT calculation, was based on the formation of a strong Zn–O bond with adsorbed alcohol molecules. A charge transfer from ethanol to sensing layer induced the electrical resistance increase. The sensor response resulted in higher N_2 atmosphere with respect to O_2 atmosphere, supporting the hypothesis that the adsorption–desorption process was mainly responsible for sensing performance, while the redox reaction of ethanol with chemisorbed oxygen species played a limited role. The use of atomically dispersed Zn allowed the 100% utilization of atom active sites. To increase the mass loaded on solid supports, preserving the atomically dispersed nature of metals could further improve sensing performance.

Composite materials made of graphitic materials and metal oxide were also investigated. For instance, the g-C_3N_4/Ag_2ZrO_3 nanocomposite was used to efficiently detect ethanol in the concentration range of 1–1000 ppm [73]. The resulting specific surface area of the g-C_3N_4/Ag_2ZrO_3 was about 136 m^2/g, which was remarkably higher than that of the pure materials components g-C_3N_4 (12.41 m^2/g) and Ag_2ZrO_3 (31.19 m^2/g). The formation of pores between the aggregate compounds favored the diffusion and adsorption of vapors on the surface. Upon exposure to 50 ppm of ethanol at room temperature, the sensors based on g-C_3N_4, Ag_2ZrO_3 and g-C_3N_4/Ag_2ZrO_3 showed responses of $(R_{gas} - R_{air}) \times 100/R_{air}$ of 15.1, 24.5, and 53.1%, respectively.

4.3. 2D Metal Chalcogenides-Based Gas Sensors

The metal chalcogenides family consists of inorganic chemical compounds made of at least one chalcogen element (S, Se, or Te) and at least one more electropositive metal element. Depending on the chemical formula and structural configuration, the metal chalcogenides exhibit metallic, semimetallic, semiconducting, or superconducting behavior.

4.3.1. 2D Transition Metal Dichalcogenide (TMDs)

The transition metal dichalcogenides (TMDs) have been intensively investigated due to their electrical and optical properties, which can be tuned through size decreasing from bulk materials to single nanolayers. The TMDs typical formula is MX_2, where M represents the transition metal atom and X the chalcogen atom. In the structure of TMDs, each layer of metal atoms is sandwiched between two layers of chalcogen atoms [74]. As a consequence, each individual sheet consists of three atomic layers. Several exfoliation methods and vapor-deposition techniques have been developed to obtain TMDs made of single or few nanosheets. The employment of TMDs in gas sensing was considered for their high sensitivity at room temperature. The sensing performance can be further improved through the creation of heterostructures.

The efficient ethanol detection achieved by using a tungsten disulfide/tungsten trioxide (WS_2/WO_3) nanocomposite was demonstrated by Zhang et al. [75]. WS_2 nanosheets and WO_3 nanoparticles were produced by using a hydrothermal process and,

subsequently, a layer-by-layer self-assembly method was used to deposit a WS_2/WO_3 film on a substrate with interdigital electrodes (Figure 9). The adhesion strength on the substrate was enhanced by applying two bi-layers of poly(diallyldimethylammonium chloride)/poly(styrene sulfonate) (PDDA/PSS).

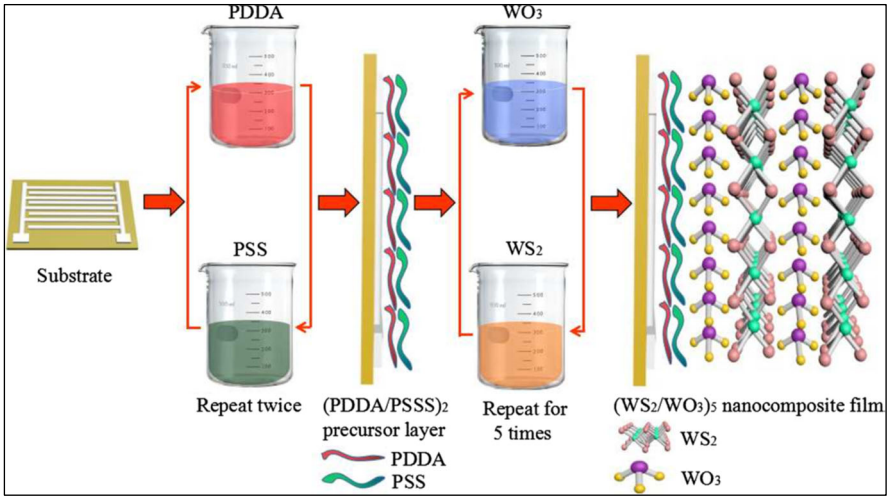

Figure 9. Schematic illustration of the layer-by-layer self-assembly of WS_2/WO_3 film (Reprinted/adapted from [75]).

The WS_2/WO_3 hybrid materials exhibited higher performances in terms of sensitivity, responses, and recovery time towards ethanol vapor with respect to pure WS_2 and WO_3. The sensing improvements were ascribed to the synergistic effects derived from the formation of WS_2/WO_3 heterojunctions.

In addition to WS_2, MoS_2 was also largely employed in gas sensing at room temperature [76]. The advantageous properties of MoS_2 include its ultra-high carrier mobility and a high adsorption capability due to the presence of edges, defects, and vacancies. Depending on the number of layers, the gap band of MoS_2 changes from 1.2 to 1.9 eV. However, MoS_2 gas sensors commonly show low sensing responses and sluggish or incomplete recovery. Improved sensing performance toward methanol at room temperature were obtained through functionalization of MoS_2 rod-shaped nanostructure with Ag nanoparticles [77]. The morphology design and the introduction of noble metal are diffused strategies to enhance sensing performances. The morphology design provides more exposed reactive sites, while the noble metals are efficient catalysts that are able to accelerate the reaction between the adsorbed oxygen species and the analyte molecules. Upon exposure to 100 ppm of methanol, the resulting sensing responses of pristine MoS_2 and functionalized MoS_2/Ag (2 wt%) were 7.1%, and 21.6%, respectively. The sensor responses were calculated using the formula $(R_{gas} - R_{air}) \times 100/R_{air}$. The higher efficiency of MoS_2/Ag sensors was ascribed to the enhanced adsorption and dissociation of oxygen molecules into oxygen ions. Therefore, more trapped electrons were created, leading to an improvement in methanol sensing. In addition, due to the excellent catalytic nature of Ag nanoparticles, the breakdown of methanol molecules in reactive radicals was facilitated.

Adopting a similar strategy, remarkable ethanol gas-sensing performances were obtained attaching, on the surface of MoS_2 nanoflowers, CeO_2 nanoparticles [78]. The advantageous intrinsic CeO_2 properties are related to the presences of a large number of oxygen vacancies and the possibility to uptake and release oxygen via the redox reaction between Ce^{3+} and Ce^{4+}. However, due to its high resistance value, pure CeO_2 is not widely employed in gas sensors. The MoS_2 functionalized with 5% CeO_2 showed improved ethanol-sensing performances in terms of sensitivity, response and recovery time, repeatability, and selectivity with respect to pristine MoS_2. The oxygen vacancies in CeO_2 increased the oxygen adsorption in the MoS_2/CeO_2 composite and, upon ethanol

exposure, more electrons were released, directly resulting in a greater conductivity. Furthermore, the MoS_2/CeO_2 composite exhibited a specific surface area of 27.36 m^2/g, while, for pristine MoS_2, a lower surface area of 15.59 m^2/g was calculated. A larger active surface area is beneficial for gas adsorption and diffusion. The formation of a n–n heterojunction also contributed to improving the ethanol-sensing performance. Due to the different work functions of MoS_2 and CeO_2, electrons moved from MoS_2 and CeO_2 until the Fermi level satisfied the equilibrium state. The charges' movements caused the formation of a depletion layer and an electron accumulation layer and, as a consequence, led to an increase in oxygen chemisorption. The thickness of electron depletion and accumulation layers decreased because of the release of electrons in the reaction between ethanol molecules and chemisorbed oxygen species. This effect of electronic sensitization is completely similar to that described in the present review for heterojunctions between MOSs.

The less investigated 2D-HfS_2 showed good sensitivity towards methanol, ranging from 100 to 500 ppm at room temperature [79]. The observed good baseline restoration in sensing tests and the recorded fast response/recovery times of 12 and 24 s, respectively, provided evidence of HfS_2's potential as a sensing material.

4.3.2. 2D Metal Monochalcogenides

Recently, 2D group IV-VI mono chalcogenides (GeS, GeSe, SnS, and SnSe) have also been investigated, being earth-abundant and environment friendly materials with low cost and high chemical stability. Unlike flat graphene sheets, the IV-VI compound monolayers present the same puckered surface of phosphorene but have higher oxidation resistance.

For instance, the p-type SnS semiconductor has a 2D structure, like black phosphorus, with a unit cell made of two corrugated SnS double layers. The small electronegativity of S atom makes easier the oxygen absorption at low temperatures with respect to MOSs. Good sensitivity values towards ethanol have been recorded by using the 2D SnS in the temperature range of 100–250 °C [80,81].

A comparative study on the gas-sensing performance of orthorhombic SnS and hexagonal SnS_2 revealed that, at room temperature, orthorhombic SnS is more suitable for detecting trace ethanol with sub-ppm level, while hexagonal SnS_2 is more suitable for detecting higher ethanol concentrations (above 50 ppm) [82]. To exclude the effect of sample geometry, SnS and SnS_2 with similar hierarchical flower-like morphologies were synthetized through solvothermal method. By using the Langmuir isotherm model, a monolayer adsorption of ethanol molecules was demonstrated in SnS-based sensors. In SnS samples, a high specific surface area of 25.35 m^2/g was measured due to their wrinkled honeycomb surface. The resulting numerous adsorption sites induced monolayer ethanol adsorption, making possible the rarefied vapor detection. The specific surface area of SnS_2 was only 8.64 m^2/g and no sensor response was observed upon exposure to ethanol concentrations below 10 ppm. The superior monolayer adsorption characteristics of SnS were also investigated by using the first-principles calculations. The efficient ethanol adsorption and charge transfer on the SnS-based sensor were ascribed to an ordered surface-electron arrangement with high orientation. With the increase of humidity, the SnS sensitivity was reduced, and, at relative humidity above 69%, no sensor response was observed.

To improve the sensing performances of tin chalcogenides at room temperature, Quin et al. proposed an innovative in-plane heterostructure of SnS/SnS_2, obtained through a thermally induced phase transition from n-type SnS_2 to p-type SnS [83]. In Figure 10a–c, TEM images clearly show the uncommon presences of sulfide and disulfide in the same plane. The introduction of grain boundaries and lattice defects was beneficial for the detection of rarefied methanol vapors at room temperature until a concentration of 100 ppb (Figure 10d). Like pure SnS, the 2D nanosheets of SnS/SnS_2 assembled in three-dimensional nanoflower structures, which favored gas diffusion and adsorption. The improved sensing performance of SnS/SnS_2 heterostructure towards methanol, with respect to the less responsive pure SnS, can be attributed to defects formed in consequence of lattice mismatch at grain boundaries between orthogonal SnS and hexagonal SnS_2. The

authors demonstrated by using the first-principles calculations the preferential adsorption of methanol molecules on these defective sites.

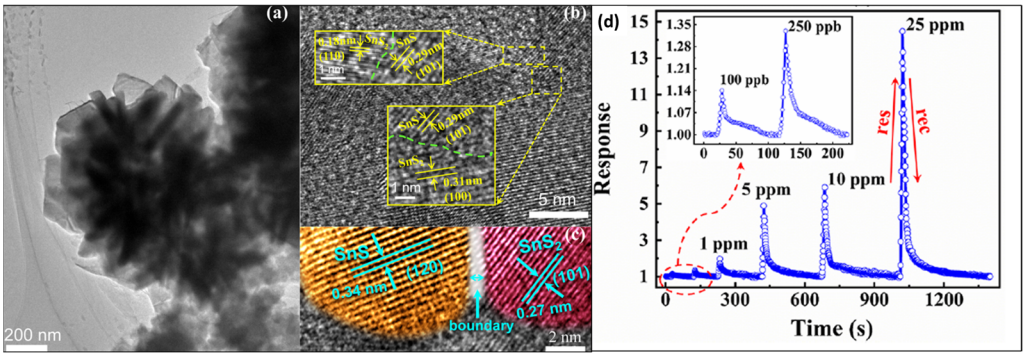

Figure 10. (**a**) TEM image of SnS/SnS_2 sheet; (**b**,**c**) HRTEM images of SnS/SnS_2 sheet; (**d**) Sensor responses to different methanol concentrations at room temperature (Reprinted/adapted from [83]).

The ultrathin SnS nanosheets spontaneously form hierarchical assembly taking the form of nanoflowers or nanospheres. With the aim of further increasing the exposed surface, Qin et al. reduced the stacking of SnS layers anchoring SnS sheets on graphene oxide (GO) by using poly(diallyl dimethyl ammonium chloride (PDDA) as electrostatic compatibilizing agent [84]. The electrostatic interaction between the cationic polymer electrolyte PDDA and the negatively charged GO allowed the attachment of SnO_3^{2-} precursor. A subsequent solvothermal treatment in presence of L-cysteine, as sulfide source, and H_2S, as reducing agent, allowed the 2D-nucleation layers of SnS and the GO reduction. The obtained SnS/rGO showed a less stacked, but highly stable architecture with good sensing performance towards methanol at room temperature. The high conductivity of rGO favored the rapid transfer of charges in the proposed sensor device. The hybrid SnS/rGO architecture provided a large active surface for gas adsorption and reaction. The sensor response, expressed as R_{gas}/R_{air}, resulted 5.2 for exposure to 15 ppm methanol. Clear sensor responses were recorded until a methanol concentration of 250 ppb. The response and recovery time resulted in 6 s and 18 s, respectively, indicating an easy diffusion process.

The same authors also demonstrated that a simple alkaline treatment with KOH solutions can make thinner the component flakes in SnS nanoflowers, further increasing the exposed active surface and facilitating diffusion and transport of analyte molecules [85]. At same time, the alkaline treatment allowed the introduction of -O function terminals on SnS surface, improving the sensing performance toward methanol. The thinning of nanoflakes was demonstrated by using XRD and XPS analysis, and was also attested to by the introduction of lattice defects, such as dislocation and micro-stress, favorable for gas adsorption. A sensor response R_{gas}/R_{air} of 3.81 was recorded upon exposure to 5 ppm of methanol, which was about 3.2 times that of untreated SnS.

As an alternative to the construction o fheterojunctions, the design of homojunctions between different crystalline phases of the same material was proposed as useful strategy to produce efficient sensors [86]. A homogeneous heterophase junction can provide an excellent lattice mismatch, thus achieving more efficient charge transfer and separation in the interface area. In this regard, the cubic/orthorhombic SnS exhibited remarkable sensing performance towards ethanol [87]. Carefully choosing the annealing temperature, the spherical cubic SnS was partially converted in block-like orthorhombic phase. The derived junction interfaces acted as high active adsorption sites.

The S-vacancy enrichment of SnS flower-like nanostructures is a further efficient strategy for remarkably improving sensing performances [88]. By using SnS with Sn/S molar ratio 4/3, a 143.9-fold increase in response value, to 5 ppm of methanol, was recorded with respect to stoichiometric SnS. The role of S defective state was investigated via first-principles calculations method. In the S-vacancy enriched SnS, the Fermi level

shifted to the conduction band, causing the decrease in hole concentrations. As a consequence, a high ratio of free carriers was available for the surface reactions with gaseous molecules. As previously described in regard to the MOSs-based sensor, defects engineering is a powerful tool to introduce coordinately unsaturated sites with the aim to tune electron density and sensor performances.

Interestingly, the decrease in hole concentration was also realized through Zn-doping [89]. Enhanced sensitivity and selectivity towards methanol was observed in Zn-substituted SnS nanoflowers with a Sn^{2+}/Zn^{2+} molar ratio of 9/1. Due to the smaller ionic radius of Zn^{2+}, the resulting ZnS bonds were shorter than the SnS bonds. The consequent stronger valence state decreased the Sn vacancy formation and the concentration of effective hole carriers. Improved responses towards methanol were ascribed to the resulting higher ratio of free carriers available for the surface reactions. Furthermore, theorical calculation of dislocation density and micro strain demonstrated the deterioration of crystal quality as a consequence of the doping with Zn^{2+} atoms. The introduced lattice defects acted as additional adsorption sites for vapor molecules. Sensors based on Zn-doped SnS showed a 32.8-fold increase in response values upon exposure to methanol with respect to pure SnS-based devices. In addition, the Zn doping led to the low detection limit of 100 ppb. Unfortunately, the response to methanol was attenuated by 23.2% after 21 days, because of ambient humidity.

The SnS modification by using Ag-doping or Ag surface functionalization was successfully employed for enhancing sensitivity and selectivity towards ethanol vapors [90]. Compared with pure SnS, the sensing response to 10 ppm ethanol of Ag-doped SnS was 3.3 times higher, while that of Ag-functionalized SnS was 4.4 times higher. Both doping and functionalization introduced, in SnS lattice, more defects, including dislocations and residual stress able to act as active sites for vapor adsorption. The best sensing performances of functionalized SnS were explained by using first-principles calculations that attested the catalytic role of metal. The Ag atoms on surface not only provided more active sites for ethanol adsorption, but also activated the adjacent Sn atoms favoring a larger charge transfer with ethanol molecules.

Recent works demonstrated the good sensitivity of PbS/SnS_2 and Au functionalized PbS/SnS_2 composites toward ethanol in the extraordinary large detection range of 60–1600 ppm [91,92]; however, the PbS is a less investigated sulfide, probably due to the high lead toxicity.

4.4. MXene Based Gas Sensors

In 2011, the large 2D materials group was further expanded with the successful synthesis of layered and conical scroll structured Ti_3C_2 [93]. The name MXene was chosen to underline the structural similarities with graphene. The MXene family includes transition metal carbide, nitride, and carbonitride with general formula $M_{n+1}X_nT_x$, where M is an early transition metal, X refers to C or N atom, and T represents the surface terminal groups not always present (such as hydroxyl, oxygen, fluorine, or chlorine) [94,95]. Currently, the Ti_3C_2 remains the most studied MXene due to its availability, exceptional tunable electronic properties, low cost, and simple fabrication methods and modification procedures [96]. The employment of MXene as sensing material was first reported by Lee et al., who demonstrated the p-type behavior of $Ti_3C_2T_x$, deposed on Pt interdigitated electrodes, upon exposure to ammonia, acetone, methanol, and ethanol vapors [97].

The MXene are commonly produced by using top-down wet etching methods, followed by intercalation and delamination processes if required. The starting reagents are MAX phases, layered ternary carbide and nitride with a general formula $M_{n+1}AX_n$, where M is an early transition metal, A is a IIIA and IVA group element and X refers to C or N atom. For instance, Ti_3C_2 MXene is usually produced by etching the Al layers out of the Ti_3AlC_2 MAX phases.

Shuck et al. demonstrated that Ti_3AlC_2 MAX phases, obtained in same conditions by using different carbon sources (graphite, titanium carbide and carbon lampblack), can be

converted in $Ti_3C_2T_x$ MXene derivatives with different flake size, morphologies, compositions, and electrical and sensing properties [98]. The highest responses upon exposure to ethanol, acetone, and ammonia were obtained with MXene derived from titanium carbide and graphite. The better sensor performances of these materials were ascribed to their higher values of conductivity that resulted in 4400 S/cm for the graphite-derived MXene and 3480 S/cm for the titanium carbide-derived MXene. The MXene derived from carbon lampblack, with a conductivity of 1020 S/cm, showed the worst gas-sensing ability.

All parameters able to affect MXene structure, morphology, and composition need further research to deeply understand the close relationship between synthesis methods and properties and, more specifically, the role of all factors involved in gas sensing. The metallic conductivity of MXene makes the gas-sensing mechanism more complicated with respect to others conventional materials. The key role of interlayer swelling was demonstrated by Koh et al., by using in situ X-ray diffraction measurements upon exposure of $Ti_3C_2T_x$ films to ethanol or CO_2 [99]. The dynamic change in interlayer distance was observed in a suitable transparent chamber in which N_2 and target gases/vapors were sequentially introduced. The N_2 exposure induced a decrease in the interlayer distance due to partial remotion of residual intercalants and water molecules. A significant MXene swelling was observed after ethanol exposure, while CO_2 introduction produced no effects. In further experiments, the $Ti_3C_2T_x$ hydrophilicity was tuned by inserting various concentrations of sodium ions into MXenes sheets. The experimental results showed swelling degrees aligned with the gas-response intensity demonstrating the crucial role of interlayer vapor diffusion in sensing mechanism. Treatment with 0.3 mM NaOH induced both the maximum swelling and the highest response toward ethanol. The amount of intercalated water molecules can be tuned to optimize gas-sensing performances, being crucial to reduce interaction between 2D sheets and to create extra space for vapors diffusion.

Gas-sensing improvements can also be achieved by designing suitable hybrid structures in which heterojunctions between MXene and other nanomaterials are introduced. A $Ti_3C_2T_x/WSe_2$ hybrid sensor, with a sensitivity towards ethanol 12 times greater than pristine $Ti_3C_2T_x$, was proposed by Chen et al. [100]. The $Ti_3C_2T_x$ MXene nanosheets and the transition metal dichalcogenide WSe_2 were both synthesized by liquid phase exfoliation. The $Ti_3C_2T_x/WSe_2$ nanohybrid was produced through a solution mixing method and then incorporated in an inject-printing and wirelessly operating flexible device (Figure 11a). The inject-printing method allowed a reproducible and fine control of thickness in deposited layers made of WSe_2 flakes of about 30 nm distributed homogenously on the edges of $Ti_3C_2T_x$ nanosheets with a typical size of 300 nm. The surface terminal groups in MXene facilitated the hybridization process with WSe_2 and the formation of numerous heterojunctions, proposed as the major adsorption sites. The $Ti_3C_2T_x/WSe_2$ heterojunctions provided fast electron transport and acted as efficient catalysts, lowering the activation energy of analyte molecules. The sensors based on $Ti_3C_2T_x$ films loaded with 2 wt% WSe_2 exhibited the highest gas responses and low values of electrical noise. Higher amounts of loaded WSe_2 resulted in worse sensing performances due to heterojunctions blocking. The sensor performances were also significantly affected by thickness of the $Ti_3C_2T_x/WSe_2$ layer. The sensor responses upon exposure to vapors decreased dramatically with increasing film thickness because of the surface/volume ratio decrease. High sensor responses were recorded by using $Ti_3C_2T_x/WSe_2$ films of 60 nm and rapid response and recovery time, of 9.7 s and 6.6 s respectively, were also observed. A further benefit, derived from $Ti_3C_2T_x$ hybridization with WSe_2, was the increased moisture resistance (Figure 11b,c). The presence of WSe_2 nanoflakes on the edges of $Ti_3C_2T_x$ nanosheets blocked the direct interaction of water molecules with MXene, reducing its high susceptibility to environmental degradation. The $Ti_3C_2T_x/WSe_2$ based sensor showed long stability and durability, also after exposure to 80% of relative humidity.

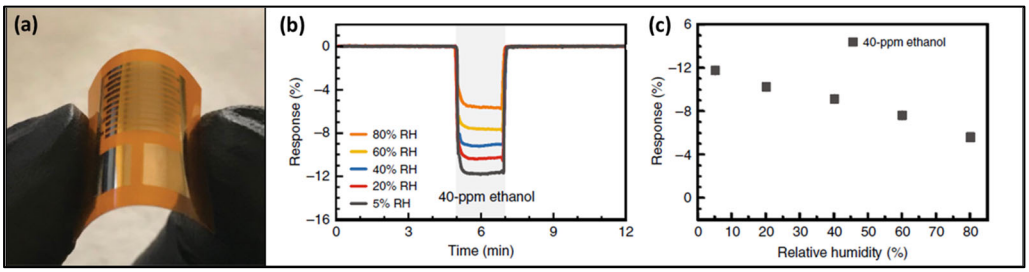

Figure 11. (**a**) Photograph of $Ti_3C_2T_x/WSe_2$ flexible sensor; (**b**) Responses of $Ti_3C_2T_x/WSe_2$ sensor to 40 ppm of ethanol under various humidity conditions; (**c**) the sensing responses as a function of relative humidity (Reprinted/adapted from [100]).

Hybridization of $Ti_3C_2T_x$ MXene with graphitic carbon nitride (g-C_3N_4) was investigated by Hou et al. [101]. The resulting composite showed excellent sensitivity to ethanol in the concentration range of 10–600 ppm at room temperature under UV irradiation. The irradiation of sensing material with sufficient intensity of light energy was used to induce the valence band electron transition generating free electrons. The heterojunction formation between MXene and g-C_3N_4 facilitated electron transport and reduced the recombination of photoelectron and holes, enhancing the sensing performance of the hybrid structure with respect to single pristine materials. The MXene lamellar structure also promoted photoelectron transportation, making them more available for reactions with adsorbed oxygen. Under vapor exposure, the ethanol molecules reacted with oxygen anions and released the electron, causing the resistance decrease. The high sensor response of 91%, expressed as $(R_{gas}\text{-}R_{air})*100/R_{air}$, was recorded upon exposure to 10 ppm of ethanol, but, in the absence of UV light irradiation, the response was 45.3%.

The construction of heterojunctions between MXenes and MOSs was also investigated [102]. In this regard, the $In_2O_3/Ti_3C_2T_x$ composite was successfully employed for methanol sensing at room temperature in the concentration range 5–100 ppm [103]. The surface of In_2O_3, having a nano-cubic geometry, was modified with the cationic surfactant (3-aminopropyl) triethoxysilane (APTES) to facilitate anchoring on $Ti_3C_2T_x$ sheets. The enhancement of $In_2O_3/Ti_3C_2T_x$ sensing performances was mainly ascribed to the formation of heterojunctions at the interface between MXene and MOS and to the mesoporous structure of composite with larger specific surface area with respect to constituent materials.

The efficient detection of isopropanol was demonstrated by using the ternary system $MoO_3/TiO_2/Ti_3C_2T_x$ with a p-type behavior synthetized by a simple one-step hydrothermal method [104]. As a result, TiO_2 and the MoO_3 nanoparticles were evenly distributed all over the layers of $Ti_3C_2T_x$ and X-ray diffraction analysis attested to an enlargement of MXene interlayer spacing after the MoO_3 introduction. The functionalization with oxides also increased the specific area of $Ti_3C_2T_x$ from 9.42 m^2/g to 66.3 m^2/g. In addition, the loading of MoO_3 significantly decreased the electrical resistance of the sensing layer, indicating an intimate electronic coupling at interface. Compared to pristine $Ti_3C_2T_x$, the efficiency of $MoO_3/TiO_2/Ti_3C_2T_x$ composite sensor towards isopropanol was remarkably improved. A sensor response of 245% was calculated with the formula $(R_{gas} - R_{air}) \times 100/R_{air}$ upon exposure to 50 ppm of isopropanol at room temperature, with response and recovery times of 100 s and 40 s, respectively. The introduction of TiO_2 and the MoO_3 nanoparticles boosted oxygen adsorption providing more active sites for the reaction with the isopropanol molecules, and the formation of an intimate heterojunction promoted the charge transfer between $Ti_3C_2T_x$ and MoO_3. An excess of loaded MoO_3 (above 30% in weight) resulted in the worst sensing performances due to the loss of layered structure in the resulting composite material.

A similar ternary system $MoO_2/MoO_3/Ti_3C_2T_x$, but with a n-type behavior, was used for the efficient detection of ethanol in the concentration range of 5–200 ppm [105].

5. Polymers

The chemical and physical properties of polymers can be tuned through the suitable choice of starting monomers and the introduction of several functional groups. As a consequence, materials with electrical conductivity across a range of about 15 orders of magnitude can be obtained, exploiting the infinite possibility offered by chemical synthesis. Among the polymeric materials, the large family of conducting polymers, having a conjugated chain structure, is the most employed in gas-sensor design. The experimentation of conducting polymers as sensing materials started in 1983 with the design of an ammonia sensor [106]. Conjugated polymers are generally not conductors at the pristine state, but the doping process or the polarization of the monomer units greatly increases conductivity due to formation of nonlinear defects such as solitons, polarons, or bipolarons. The electrical conductivity is related either to the charge-carrier mobility along polymer chain or to the charges hopping between different neighboring polymer chains. The facile processability and the mechanical flexibility of polymeric materials allow their easy integration into low-cost and portable sensing devices.

Polymeric sensing layers can be realized by simple drop-casting methods, as reported by Samanta et al. for the poly(*o*-phenylenediamine) with amine (-NH_2) functional group substitutions [107]. After doping with sulfuric acid, this polymer was used as chemiresistor for the successful sensing of ethanol and ethanol/methanol or ethanol/isopropanol mixtures. The hydrogen-bond formation between alcohol molecules and polymer induced the decrease of electrical resistance.

The main limits of semiconductor polymers for sensing application are generally their low sensitivity, poor stability, and unsatisfactory selectivity. Sensing performances can be enhanced by using several strategies including functionalization, increasing the surface area, redox doping, or the fabrication of multicomponent composites.

In some cases, non-conjugated polymers are also employed in sensor devices. For instance, the organic–inorganic ternary nanohybrid, consisting of oxidized-single walled carbon nanohorns-SnO_2-polyvinylpyrrolidone (ox-SWCNH/SnO_2/PVP), was used as chemiresistive materials for ethanol sensing [108]. The PVP was selected as sensing material for its polar groups useful to promote alcohol adsorption. In addition, the polymer was used as a binder, having good adhesion to the solid substrate, and as a dispersing matrix for the carbonaceous nanomaterials. The SWCNHs are carbon conical-horn shaped nanostructure made of graphene sheets that are difficult to fix on a substate due to their poor adherence and low processability. The ternary ox-SWCNH/SnO_2/PVP composite showed excellent sensitivity towards ethanol concentrations below 2 mg/L, with response and recovery times of 30 s and 50 s, respectively. An analogous SWCNH/ZnO/PVP ternary composite was also synthetized and tested, but the worst sensing performances were recorded.

Polyaniline (PANI)-Based Gas Sensors

Among conducting polymers, polyaniline (PANI) has been largely employed in gas sensors devices, being an inexpensive, highly conductive, and stable material prepared through simple methods [109,110]. In addition, PANI exhibits three isolable oxidation states that can be transformed into each other by redox (Figure 12). The leucoemeraldine form is totally reduced and includes only benzenoid structural units. The half-oxidized emeraldine and the fully oxidized pernigraniline includes benzenoid and quinoid structural units. The emeraldine can be converted into electrically conducting (emeraldine salt) or non-conducting (emeraldine base) form through a reversible acid/base doping process (Figure 12b,c). In summary, unlike most conjugated polymers, the PANI conductivity can be easily controlled by both redox and acid/base reactions.

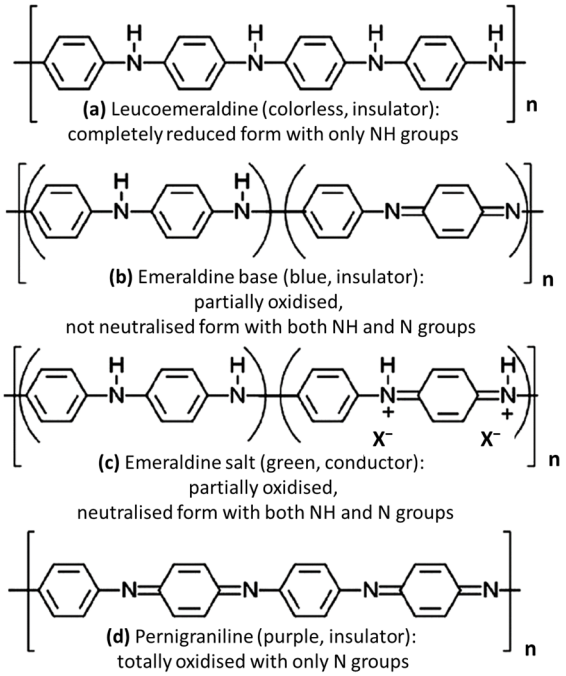

Figure 12. Oxidation states of polyaniline.

In order to obtain improvements of sensing properties, PANI was commonly mixed to several reinforcements, such as MOSs or 2D materials. For instance, the efficient detection of methanol at room temperature was demonstrated by using a PANI/graphene composite fabricated through a hydraulic press in forms of pellets with diameter of 13 mm and thickness of 0.4 mm [111]. The sample exhibited an agglomerated macro-structure, shown in Figure 13a, probably derived from a polymerization process started on graphene sheets. Two silver electrodes were directly applied on the pellets' surface. The composites with graphene weight percentage of 8% showed a high response of 61.5%, calculated as $(I_{gas} - I_{air}) \times 100/I_{air}$, upon exposure to 100 ppm of methanol.

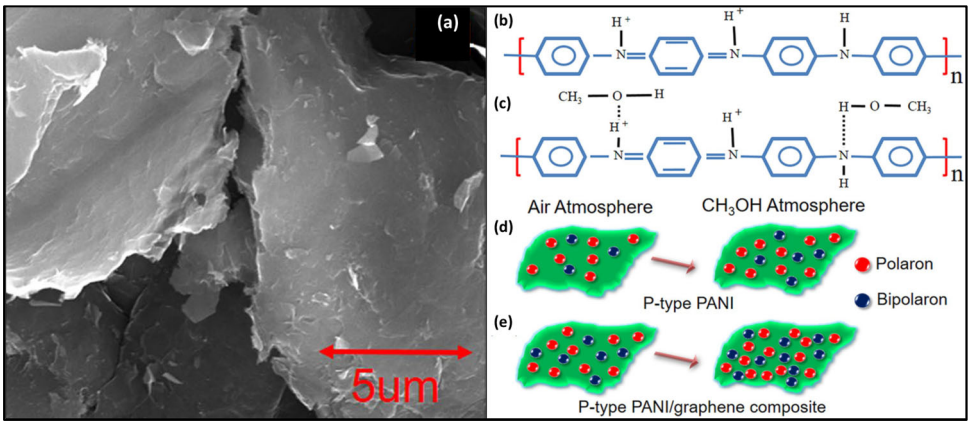

Figure 13. (**a**) FESEM images of PANI/graphene composite; (**b**) PANI chain; (**c**) hydrogen bond formation between PANI and methanol molecules; (**d**,**e**) PANI and PANI/graphene composite under methanol environment from air environment (Reprinted/adapted from [111]).

The mechanism of gas sensing in PANI is strictly related to its peculiar redox chemistry, and different sensor responses can be obtained for doped and undoped states upon exposure to the same analyte vapors. Methanol molecules can interact with both the emeraldine salt and base forms of PANI, causing opposite changes in conductivity. In both cases, the basic mechanism involves the formation of hydrogen bonds, in both cases,

the basic mechanism involves the reversible formation of hydrogen bonds [112]. The electrical conductivity of the emeraldine base form of PANI decreases upon exposure to methanol. In this case, the nitrogen lone pair on the quinoid moieties and the NH group of benzenoid moieties forms hydrogen bonds with the hydrogen atom and the oxygen lone pairs of the methanol hydroxyl groups, respectively. As a consequence, the methanol molecules can act as bridging units between the polymer chains, twisting them away from a planar geometry. The consequent localization of polarons in a range of few monomer units decreases conductivity. On the contrary, the electrical conductivity of the emeraldine salt form of PANI increases upon exposure to methanol. In this case the nitrogen atoms on the quinoid moieties are protonated and the methanol molecules are unable to bridge the polymer chains. The conductivity increase can be ascribed to formation of new polaron units due to interaction with methanol molecules.

The increase in electric current upon methanol exposure in the PANI/graphene composite was attributed to presence of emeraldine salt form and to increase of polarons concentration. The performed XRD and Raman analysis provided further evidence of emeraldine salt formation in PANI/graphene. The improved sensing responses towards methanol, with respect to pure PANI, were ascribed to several factors including the higher polarons concentrations, the enhanced surface-to-volume ratio, due to the 2D nature of graphene, and to the high graphene conductivity that favored charge-carrier mobility inside the whole composite. The schematic sensing mechanism for PANI and rGO-PANI nanocomposites is reported in Figure 13b–e. The negligible effect of moisture on gas-sensing performances was also demonstrated in relative humidity ranging from 10 to 90%.

Recent publications highlighted the interesting synergistic properties have emerged in regard to PANI/rGO composites [113,114] and Kumar et al. demonstrated the efficiency of PANI/rGO as sensing material to methanol detection [115]. Also, in this case, the sensor was fabricated pressing the pristine rGO-PANI nanoparticles with a hydraulic machine in the form of pellets. Different rGO concentrations were investigated in the range 0–8 wt%. The addition of rGO enhanced the porosity of polyaniline increasing gas-adsorption capacity. Ranging the content of rGO particles from 0 to 8% by weight, the specific surface area grew from 14.465 to 33.2454 m^2g^{-1}. From the analysis of Raman spectra, the area associated with quinoid (A_Q) and benzenoid (A_B) moieties in PANI polymeric chains were computed. The A_Q/A_B ratio increased from 0.39 to 0.80 with an increase of rGO concentration from 0 to 8 wt%. Higher values of A_Q/A_B ratio correspond to higher values of conjugation length and electrical conductivity. Due to the enhanced conductivity, the 8 wt% rGO doped polyaniline exhibited the maximum responses upon methanol exposures in the concentration range 50–200 ppm. The increase of rGO-PANI electrical conductivity, respect to pristine PANI, was related to the increase of charge carrier concentrations (polarons and bipolarons). Following interaction with alcohol molecules, further charges were produced as described for PANI/graphene composites (Figure 13b–e). A slight increase in sensor responses was recorded with the increase of relative humidity until 90%. The interaction between PANI lone pairs and water molecules increased both the p-type character of polymeric chains and their electrical conductivity.

The same authors demonstrated the efficient sensing properties of porous activated charcoal (AC) and PANI composites towards methanol [116]. The PANI loaded with an AC weight percentage of 20% exhibited the maximum sensing response of 42.54%, calculated with the formula $(I_{gas}\text{-}I_{air})*100/I_{air}$ at a methanol level of 200 ppm. Also, in this case, the enhancement in current, observed in presence of methanol vapor, was ascribed to an increased concentration of polarons and bipolarons. The improved sensing responses of composite with respect to pure PANI were associated with the increased surface-to-volume ratio, arising from AC morphology, and with AC conductivity able to favor charge-carrier mobility. The humidity had no significant effect on the sensing ability of PANI/AC composites.

For their advantageous properties, including the ability to interact with small molecules and the tunable energy band gap, graphene quantum dots (GQDs) are considered alternative promising additives useful to enhance sensing performances of

polymers. Graphene quantum dots (GQDs) consist of a monolayer or few layers of graphene with lateral dimension of less than 100 nm [117]. For instance, the employment of nitrogen-doped graphene quantum dots (NGQDs) as PANI reinforcement allowed for designing an efficient sensor for ethanol and isopropanol vapors [118]. The sensors were fabricated from a PANI/NGQDs solution by drop-casting on gold interdigitated electrodes. The PANI/NGQDs exhibited higher conductivity and higher specific surface area compared to bare PANI. The introduction of NGQDs provided higher charge transfer pathways and contributed to increased surface area and adsorption sites, thus improving sensing capability.

The ternary system α-Fe_2O_3/PANI/PbS also showed excellent sensing performance towards methanol at room temperature [119]. The α-Fe_2O_3 was synthetized in the form of urchin-shaped hollow microsphere with beneficial properties for sensing application such as the large specific surface area, the presence of clear internal voids, the low density, and the good surface permeability. The α-Fe_2O_3/PANI composite thin-film sensor was obtained by spinning a suitable solution uniformly on an epoxy substrate with interdigitated electrodes. The PdS quantum dots were deposited by a successive ionic layer adsorption and reaction (SILAR) method. The methanol-sensing responses of the α-Fe_2O_3/PANI and the α-Fe_2O_3/PANI/PbS-based sensors were recorded in the concentration range of 10–100 ppm (Figure 14a). Upon exposure to 10 ppm of methanol, the α-Fe_2O_3/PANI and the α-Fe_2O_3/PANI/PbS-based sensors exhibited response values (R_{air}/R_{gas}) of 1.12 and 1.55, respectively. The hollow microspherical structure of α-Fe_2O_3 and the hydrogen-bond formation between methanol and PANI nitrogen atoms played a crucial role in a sensing mechanism favoring the surface–vapor interaction. The PbS quantum dots furnished further active sites on the surface able to react with methanol molecules (Figure 14b).

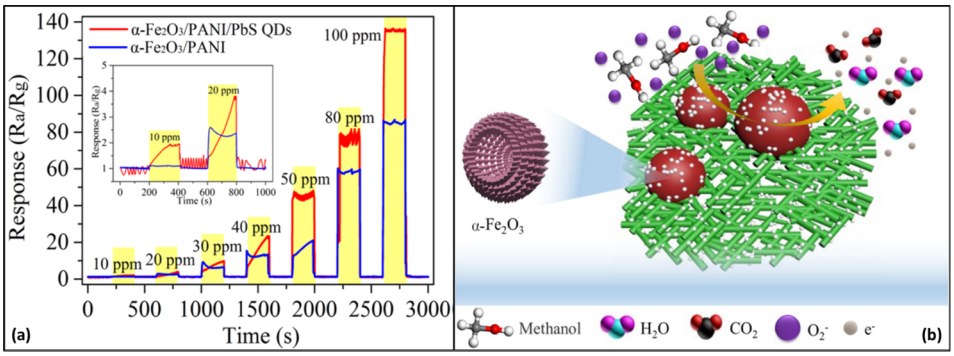

Figure 14. (**a**) Sensor responses to methanol at room temperature; (**b**) Schematic illustration of α-Fe_2O_3/PANI/PbS gas sensor mechanism (Reprinted/adapted from [119]).

A further example of PANI/MOS composite was obtained introducing V_2O_5 during PANI polymerization [120]. The high sensing responses of PANI/V_2O_5, observed toward methanol, were ascribed to the enhanced aspect (surface/volume) ratio and to the changes of charges concentration and mobility due to the formation of p–n junctions between the p-type polyaniline and the n-type V_2O_5.

6. Gasistor

Metal oxide-based resistive gas sensors usually present unstable baseline, due to resistance drift in time, and require high operating temperature, having low sensitivity and long recovery time at room temperature. The possibility to overcome these problems through the design of memristors for gas sensing, named gasistors, was recently demonstrated by different groups of researchers [121–123]. The memristor or resistive random-access memory (RRAM) is a non-linear resistor with peculiar resistive switching functions conventionally used for nonvolatile memory. The memristor structure is usually composed of an oxide active layer between two metallic electrodes. The transition metal oxides are the most-used materials, generally in filaments form. The resistive switching

mechanism involves the formation and dissolution of conductive filaments (CFs) inside the active layer, as a consequence of the redox reactions induced by applying an intense electric field [124]. The formation of CFs allows for reaching the low resistance state (LRS), while, in the high resistance state (HRS), the CFs are partially dissolved. In both the HRS and the LRS state, the memristor exhibits lower resistance values with respect to pristine state. The use of 1D and 2D materials in memristors have been intensively investigated to control the formation process of conductive channels [125,126]. The 1D structure materials are particularly advantageous for their high surface/volume ratio, their controlled charge transportation pathway, and for their potential in developing miniaturized devices.

Qui et al. described a gasistor with SnS-modified TiO_2 nanowires able to detect methanol in the range of 250 ppb–5 ppm at room temperature (Figure 15) [127].

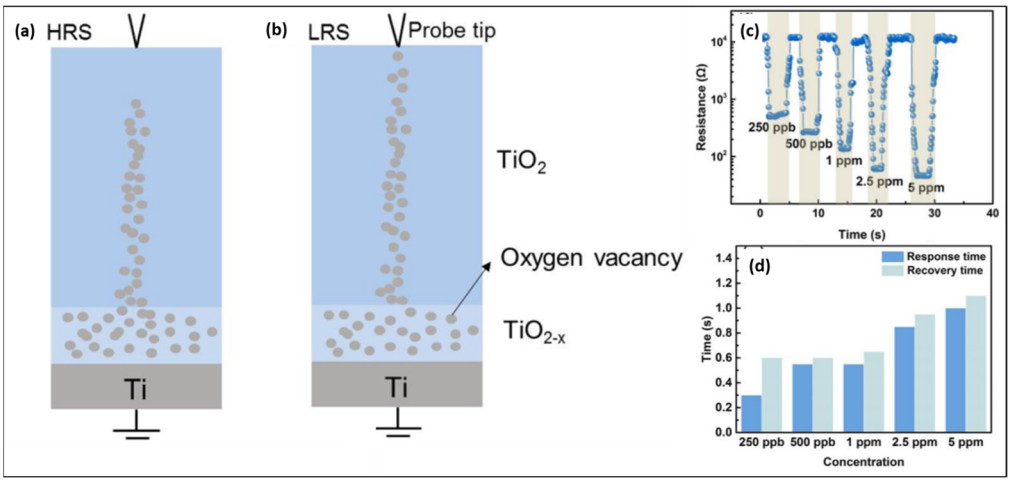

Figure 15. Schematic illustration of the SnS/TiO_2-based gasistor in (**a**) HRS and (**b**) LRS. (**c**) Response to different methanol concentrations in HRS. (**d**) Response and recovery time to different methanol concentrations. (Reprinted/adapted from [127]).

The baseline resistance was reduced by about 3×10^4 times, showing the great advantage of memristors respect to conventional resistive devices. The reduction of baseline resistance improves the signal-to-noise ratio, and as a consequence, higher sensitivity and lower detection limits can be reached. The choice of a 1D nanowires structure allowed for obtaining rapid dynamic response and recovery, inferior to 1.2 s, as shown in Figure 15d, without resorting to the application of pulse bias, as proposed by Zhang and coworkers [119]. The 1D structure was also useful to obtain a stable switching performance, providing a direct pathway for ionic migration. The deposition of SnS on TiO_2 enhanced sensitivity and selectivity towards methanol, due to the presence of S vacancies. A rapid drop in sensor response was observed for relative humidity values higher than 65%, probably as a consequence of adsorption of the water molecules on the active sites of the SnS/TiO_2 layer.

Similarly, a gasistor based on indium gallium zinc oxide (IGZO) was employed in isopropanol sensing [128]. A remarkable response of 55.15, calculated with the formula R_{gas}/R_{air}, was recorded upon exposure to 50 ppm of isopropanol with a response time of 105 s. A slow recovery time of 543 s was observed; nevertheless, restoration of the initial state was possible in 50 μs by also applying a pulsed voltage in the presence of isopropanol vapors. A mobile device was used to determinate the isopropanol concentration in the test chamber, by acquiring, in real-time, the resistance changes of gasistor.

A SnO_2-based gasistor was also efficiently used for isopropanol-sensing in the concentration range of 10–30 ppm [129] Although there are still few gasistors described in the literature, their advantageous properties that have emerged, such as the low power consumption, the simple structure, and the ease of operation characteristics, offer new opportunities to design innovative gas sensors based on the resistive switch phenomena.

7. Discussion and Future Perspectives

We reviewed families of materials with the best sensing performances towards alcohols at room temperature, focusing attention on scientific advances and innovations published in the span of the last five years. The presented list, summarized in Table 2, cannot be considered totally exhaustive and complete, but provides a useful tool for comparing the most-investigated sensing materials. However, it is worth noting that the gas test conditions, including exposure time and gas flow systems (static or continuous), significantly vary from publication to publication.

Table 2. Summary of reviewed sensitive materials used for alcohol detection at room temperature.

Material	Morphology	Alcohol	Sensitivity	Sensing Range	Response Time	Recovery Time	Refs.
			MOSs				
Bi_2WO_6	Silkworm pupae-like cages	Isopropanol	R_{air}/R_{gas} 3.8 (500 ppm)	10–500 ppm	18 s	117 s	[25]
AAO	Nanoporous	Ethanol	$(R_{gas} - R_{air}) \times 100/R_{air}$ 61.5% (100 ppm)	100–1000 ppm	-	-	[27]
ZnO	Nanobristles	Ethanol	R_{air}/R_{gas} 464 (100 ppm)	50–150 ppm	20 s	12 s	[28]
TiO_2	Flower-like microstructures	Ethanol	R_{gas}/R_{air} 2.25 (100 ppm)	10–500 ppm	-	-	[29]
NiO/SnO_2	Nanoparticles	Ethanol	R_{air}/R_{gas} 140 (100 ppm)	1–150 ppm	23 s	13 s	[31]
ZnO/NiO	Nano-worm	Ethanol	$(R_{air} - R_{gas}) \times 100/R_{air}$ 32.48% (250 ppm)	250–1500 ppm	2.7 s	3.6 s	[32]
ZnO/GaN	Flower-like	Ethanol	R_{air}/R_{gas} 26.9 (50 ppm)	0.1–50 ppm	12 s	9 s	[33]
NiO/CeO_2	Nanoparticles	Isopropanol	R_{air}/R_{gas} 1570 (100 ppm)	1–100 ppm	15 s	19 s	[34]
α-Fe_2O_3/Ag	Nanoparticles	Ethanol	$(R_{gas} - R_{air})/R_{air}$ 4.5 (35 mg L^{-1})	2–35 mg L^{-1}	17 s	33 s	[35]
TiO_2	Nanotubes/nanoparticles	Ethanol	$(R_{air} - R_{gas}) \times 100/R_{air}$ 57.0% (100 ppm)	1–100 ppm	30 s	16 s	[36]
F-doped SnO_2	Hollow nanofibers	Ethanol	R_{air}/R_{gas} 5.53 (100 ppm)	10–100 ppm	85 s	145 s	[37]
Ce-doped $LaCoO_3$	Nanoparticles	Ethanol	Z_{gas}/Z_{air} 231 30%	10–40%	16 s	8 s	[38]
ZnO	Porous fractals	Ethanol	$I_{gas}/I_{air} - 1$ 4.3	0.01–1 ppm	11 min	12 min	[42]

			(1 ppm)				
ZnO oxygen vacant	Porous fractals	Ethanol	$I_{gas}/I_{air} - 1$ 10.41 (1 ppm)	0.01–1 ppm	300 s	360 s	[42]
APTES-WO_{3-x}	Nanowires	Ethanol	R_{air}/R_{gas} 2.0 (10 ppm)	10–80 ppm	2.8 min	-	[43]
CuO/C	Nanoparticles / nanosheets	Ethanol	$(R_{gas} - R_{air}) \times 100/R_{air}$ 3500% (3400 ppm)	170–3400 ppm	105 s	18 s	[52]
SnO_2	Nanocubes	Butanol	$(R_{gas} - R_{air}) \times 100/R_{air}$ 175% (100 ppm)	1–500 ppm	184 s	183 s	[53]
Au/SnO_2	Nanocubes	Butanol	$(R_{gas} - R_{air}) \times 100/R_{air}$ 240% (100 ppm)	0.25–500 ppm	290 s	450 s	[54]
Fe_2O_3/rGO	Nanocubes	Butanol	$(R_{air} - R_{gas}) \times 100/R_{air}$ 171% (100 ppm)	10–100 ppm	53 s	42 s	[55]
SnS/TiO_2	Nanowires	Methanol	R_{air}/R_{gas} 85.2 (1 ppm)	0.250–5 ppm	1.2 s	1.2 s	[127]
IGZO	Film	Isopropanol	R_{gas}/R_{air} 55.15 (50 ppm)	10–50 ppm	105 s	543 s	[128]
SnO_2	Film	Isopropanol	R_{gas}/R_{air} 2.02 (30 ppm)	10–30 ppm	4 s	6 s	[129]
			MOFs				
SnS/ZIF-8	Flower like	Methanol	$G_{air}/G_{gas} - 1$ 68.65 (10 ppm)	1–10 ppm	8 s	30 s	[48]
ZIF-8& Ag@SiNWs	Nanosphere/ Nanowires	Ethanol	R_{air}/R_{gas} 3.0 (10 ppm)	0.125–50 ppm	5.5 s	45 s	[49]
Ni_2[CuPc$(NH)_8$] -OTMS	Thin film	Methanol	$(I_{gas} - I_{air}) \times 100/I_{air}$ 3.22% (400 ppm)	10–500 ppm	36 s	13 s	[51]
			2D materials				
rGO	Nanosheets	Ethanol	I_{gas}/I_{air} 100 (25 ppm)	25–150 ppm	2 s	17 s	[57]
GONRs	Nanoribbons	Ethanol	$(R_{gas} - R_{air}) \times 100/R_{air}$ 4.4% (100 ppm)	100–680 ppm	-	-	[58]
SnO_2/rGO	Nanoparticles /nanosheets	Ethanol	R_{air}/R_{gas} 12.0 (145 ppm)	29–145 ppm	123 s	128 s	[60]
SiO_2/GO	Nanoparticles	Ethanol	$(G_{gas} - G_{air})/G_{air}$ 9.5 (50 ppm)	10–50 ppm	-	-	[61]

MoO_2-Ni-graphene	Hierarchical structure	Ethanol	R_{gas}/R_{air} 105 (1000 ppm)	15–1000 ppm	-	-	[62]
CNTs/Co_3O_4@rGO	Mesopours structure	Ethanol	$(R_{gas} - R_{air}) \times 100/R_{air}$ 1.36% (50 ppm)	10–150 ppm	-	-	[63]
Graphene-Cu BTC	Sheets/nanoparticles	Methanol	$(R_{gas} - R_{air})/R_{air}$ 0.15 (22.6 ppm)	2.82–22.6 ppm	-	-	[64]
Graphene-based Ink	Nanosheets in fractal architecture	Ethanol	$(R_{gas} - R_{air}) \times 100/R_{air}$ 12% (30 ppm)	5–100 ppm	6 s	36 s	[65]
Exfoliated graphene and rGO	Nanoflakes	Methanol Ethanol Isopropanol	$(Z_{gas} - Z_{air})/Z_{air}$ 0.9 (80 ppm) 2.5 (80 ppm) 1.2 (80 ppm)	10–80 ppm	-	-	[66]
g-C_3N_4/GNPs	Nanosheets/nanoplatelets	Ethanol	$(R_{gas} - R_{air}) \times 100/R_{air}$ 125% (10 ppm)	1–10 ppm	-	-	[69]
Zn-Nitrogenated graphene	Nanosheets	Ethanol	$(R_{gas} - R_{air})/R_{air}$ 0.25 (1500 ppm)	50–1500 ppm	102 s	550 s	[70]
g-C_3N_4/Ag_2ZrO_3	Nanosheet/nanoparticles	Ethanol	$(R_{air} - R_{gas}) \times 100/R_{air}$ 53.1% (50 ppm)	1–100 ppm	-	-	[73]
WS_2/WO_3	Nanosheets/nanoparticles	Ethanol	$(R_{gas} - R_{air}) \times 100/R_{air}$ 75.50% (10 ppm)	0.001–50 ppm	54 s	26 s	[75]
MoS_2/Ag	Nanorods/nanoparticles	Methanol	$(R_{air} - R_{gas}) \times 100/R_{air}$ 21.6% (100 ppm)	30–1500 ppm	240 s	1100 s	[77]
MoS_2/CeO_2	Nanoflowers/nanoparticles	Ethanol	R_{air}/R_{gas} 5.5 (30 ppm)	1–50 ppm	7 s	5 s	[78]
HfS_2	Flakes	Methanol	$(I_{gas} - I_{air})/I_{air}$ 1.29 500 ppm	100–500 ppm	12 s	24 s	[79]
SnS	Flower like	Ethanol	R_{gas}/R_{air} 1.13 (0.5 ppm)	0.5–200 ppm	2 s	3 s	[82]
SnS/SnS_2	Flower like	Methanol	R_{gas}/R_{air} 14.85 (25 ppm)	0.1–25 ppm	8 s	-	[83]
SnS/rGO	Nanosheets	Methanol	R_{gas}/R_{air} 5.2 (12 ppm)	0.25–20 ppm	6 s	18 s	[84]
SnS	Nanoflakes	Methanol	R_{gas}/R_{air} 3.81 (5 ppm)	0.3–10 ppm	-	-	[85]
Cubic/orthorhombic SnS	Spherical	Ethanol	$(R_{gas} - R_{air}) \times 100/R_{air}$ 241%	0.5–10 ppm	6 s	9 s	[87]

SnS sulfur vacant	Flower-like	Methanol	(10 ppm) $(R_{gas} - R_{air}) \times 100/R_{air}$ 61.2% (0.5 ppm)	0.5–20 ppm	3 s	7 s	[88]
Zn-doped SnS	Flower-like	Methanol	$(R_{gas} - R_{air}) \times 100/R_{air}$ 62% (1 ppm)	0.1–10 ppm	5 s	5 s	[89]
Ag-doped SnS	Flower-like	Ethanol	$(R_{gas} - R_{air}) \times 100/R_{air}$ 58% (10 ppm)	1–10 ppm	19 s	36 s	[90]
Ag-functionalized SnS	Flower-like	Ethanol	$(R_{gas} - R_{air}) \times 100/R_{air}$ 73% (10 ppm)	1–10 ppm	16 s	53 s	[90]
PbS/SnS_2	Nanoparticles	Ethanol	$(R_{gas} - R_{air}) \times 100/R_{air}$ 45.64% (60 ppm)	60–1600 ppm	104 s	84 s	[91]
Au-functionalized PbS/SnS	Nanoparticles	Ethanol	$(R_{gas} - R_{air}) \times 100/R_{air}$ 55% (60 ppm)	60–1600 ppm	40 s	65 s	[92]
$Ti_3C_2T_x$	Flakes	Ethanol	$(R_{gas} - R_{air}) \times 100/R_{air}$ 0.1–0.2%	100 ppm	-	-	[98]
$Ti_3C_2T_x$	Flakes	Ethanol	$(R_{gas} - R_{air}) \times 100/R_{air}$ 9.995%	1000 ppm	-	-	[99]
$Ti_3C_2T_x/WS_2$	Nanoflakes/nanosheets	Ethanol	$(R_{gas} - R_{air})/R_{air}$ 9.2 (40 ppm)	1–40 ppm	9.7 s	6.6 s	[100]
TiO_2-$Ti_3C_2T_x$/g-C_3N_4	Flakes	Ethanol	$(R_{gas} - R_{air}) \times 100/R_{air}$ 91% (10 ppm)	10–600 ppm	-	-	[101]
TiO_2/TiC	Nanoparticles /nanosheets	Ethanol	$(R_{gas} - R_{air}) \times 100/R_{air}$ 32% (10 ppm)	0.01–60 ppm	2.0 s	2.2 s	[102]
$In_2O_3/Ti_3C_2T_x$	Nanocubes/nanosheets	Methanol	$(R_{air} - R_{gas}) \times 100/R_{air}$ 29.6% (5 ppm)	5–100 ppm	6.5 s	3.5 s	[103]
$MoO_3/TiO_2/Ti_3C_2T_x$	Nanoparticles /nanosheets	Isopropanol	$(R_{gas} - R_{air}) \times 100/R_{air}$ 245% (50 ppm)	1–100 ppm	100 s	40 s	[104]
$MoO_2/MoO_3/Ti_3C_2T_x$	Nanosheets	Ethanol	R_{air}/R_{gas} 2.07 (5 ppm)	5–200 ppm	46 s	276 s	[105]
Polymers							
Poly(*o*-phenylenediamine)	Thin film	Ethanol	$(R_{air} - R_{gas}) \times 100/R_{air}$ 29% (130 ppm)	87–328 ppm	8 min	18 min	[107]
ox-SWCNH/SnO_2/PVP	Thin film	Ethanol	(Rgas − Rair)/(RairΔC) 0.0022	2–50 mg/mL	30 s	50 s	[108]
PANI/graphene	Micro/nano structures	Methanol	$(I_{gas} - I_{air}) \times 100/I_{air}$ 61.5% (100 ppm)	50–100 ppm	60 s	-	[110]
PANI/rGO	Nanoparticles	Methanol	$(I_{gas} - I_{air}) \times 100/I_{air}$	50–200 ppm	30 s	100 s	[115]

PANI/activated charcoal	Nanoparticles	Methanol	52.0% (200 ppm) $(I_{gas} - I_{air}) \times 100/I_{air}$	50–200 ppm	25 s	305 s	[116]
PANI/N-doped GQDs	Nanofibrous morphology	Ethanol	42.54% (200 ppm) $(R_{air} - R_{gas}) \times 100/R_{air}$	50–150 ppm	80 s	62 s	[118]
α-Fe_2O_3/PANI/PbS	Thin film	Methanol	0.66% (100 ppm) R_{air}/R_{gas}	10–100 ppm	-	-	[119]
PANI/V_2O_5	Nanoparticles	Methanol	1.55 (10 ppm) $(R_{gas} - R_{air}) \times 100/R_{air}$	40–60 ppm	240 s	260 s	[120]
			36.41% (60 ppm)				

Future alcohol-sensitive materials must, clearly, involve sensitivity, selectivity, and stability, but they must also involve easy, green, and inexpensive preparation methods and have low energy consumption. Safety aspects must necessarily be considered mainly to produce wearable sensors or for real-time measurements of alcohol vapors in breath. In addition, environmental aspects, including the low power consumption, the amount of produced waste, and the use of nonpolluting chemical products, cannot be overlooked considering the growing need for sustainable development. Despite the great commercial success of sensor devices, there is significant room for advancement, mainly related to new materials that are able to increase sensitivity, improve reliability and, at same time, reduce costs and power consumption.

The main strategies described in the present review used to overcome the limits of each class of materials can inspire future research.

Powerful tools with large margins for improvement are as follows as:

- morphology design and synthesis of ultra-porous nanostructures;
- design of suitable heterojunctions between two dissimilar materials or homojunctions between different crystalline phases of the same material;
- doping;
- defect engineering.

The morphology design provides optimization of exposed reactive sites, and the synthesis of ultra-porous nanostructures facilitates the deep reversible penetration of target gas molecules. As a consequence, deeper layers, and not just the surface, can be involved in the gas-sensing process.

The heterojunction between two dissimilar semiconducting materials consists of an intimate electrical contact able to promote charge transfer and the formation of a charge-depletion layer. Phase modulation engineering can also be used to design homojunctions between different crystalline structures of the same material with the aim of increasing the interface adsorption sites and enhancing carrier transport and diffusion. The heterophase junction can be considered a peculiar form of heterojunction.

The dopant introduction also origins more adsorption/desorption sites and allows for the tuning of electrical properties, depending on the concentrations and dispersion state.

Defect engineering provides coordinately unsaturated sites that are able to boost molecular chemisorption and activation and to modify electron density.

In addition, a new research direction for MOSs employment is offered by gasistors, namely, memristors-based gas sensors. The baseline resistance of MOSs is unstable and huge at room temperature, limiting their low-power consumption applications. However, conventional metal oxides, such as TiO_2 or ZnO, can be used at room temperature in gasistors.

8. Conclusions

The development of low-cost efficient sensors for alcohol detection and analysis has great relevance in many fields including industrial-process control, environmental protection, and chemical safety. Sensitivity towards extremely poor concentrations and low power consumption are key factors in the design of portable and wearable devices, and to further extend their application in emerging areas such as the internet of things (IoT) and self-monitoring medical devices. The stability and lifetime of sensors is greatly affected by high operating temperature, and the detection of flammable analytes like alcohols leads to ignition risk in presence of heaters. As a consequence, the possibility of operating at a low temperature needs to be considered to reduce costs and improve safety. We reviewed the remarkable progress that has been made in regard to alcohol sensing at room temperature by using MOSs, MOFs, 2D materials, and polymers. Among the large class of 2D materials, we focused attention on graphene-based materials, graphitic carbon nitride, transition metal chalcogenides, and MXenes. To overcome the limits of each class of materials, several strategies have been proposed and described, including the fabrication of ultra-porous nanostructures, the introduction of suitable heterojunctions, doping, and defect engineering. We mainly described materials for electrical devices, but significant examples of gasistors for efficient alcohol sensing were also reported. Gasistors offer the possibility to enhance sensing performances of conventional metal oxides, such as TiO_2 or SnO_2, at room temperature.

Although much progress has been made, further improvements are required, mainly regarding long-term stability and moisture resistance to operate in ambient conditions, to produce a new generation of chemical sensors working at room temperature, and to address practical wearable applications.

Author Contributions: Conceptualization, A.M.L. and M.P.; data curation, A.M.L. and M.P.; writing—original draft preparation, A.M.L. and M.P.; writing—review and editing, A.M.L. and M.P.; visualization, A.M.L. and M.P.; supervision, A.M.L. and M.P. All authors have read and agreed to the published version of the manuscript.

Funding: This research received no external funding.

Acknowledgments: The authors would like to thank the colleague Gennaro Cassano for technical assistance in the experimental measurements.

Conflicts of Interest: The authors declare no conflicts of interest.

References

1. Boroujerdi, R.; Abdelkader, A.; Paul, R. State of the art in alcohol sensing with 2D materials. *Nano-Micro Lett.* **2020**, *12*, 33. https://doi.org/10.1007/s40820-019-0363-0.
2. Alsaigh, R.A.; Rahman, S.; Alfaifi, F.S.; Al-Gawati, M.A.; Shallaa, R.; Alzaid, F.; Alanazi, A.F.; Albrithen, H.; Alzahrani, K.E.; Assaifan, A.K. Detection of volatile alcohol vapors using PMMA-coated micromechanical sensors: Experimental and quantum chemical DFT analysis. *Chemosensors* **2022**, *10*, 452. https://doi.org/10.3390/chemosensors10110452.
3. Gallego Martinez, E.E.; Matias, I.R.; Melendi-Espina, S.; Hernaez, M.; Ruiz Zamarreno, C. lossy mode resonance based 1-butanol sensor in the mid-infrared region. *Sens. Actuators B Chem.* **2023**, *388*, 133845. https://doi.org/10.1016/j.snb.2023.133845.
4. Song, G.; Qin, T.; Liu, H.; Xu, G.B.; Pan, Y.Y.; Xiong, F.X.; Chen, Z.D. Quantitative breath analysis of volatile organic compounds of lung cancer patients. *Lung cancer* **2010**, *67*, 2, 227–231. https://doi.org/10.1016/j.lungcan.2009.03.029.
5. Luo, S.; Wang, R.; Wang, L.; Qu, H.; Zheng, L. Breath alchol sensor based on hydrogel-gated graphene field-effect transistors. *Biosens. Bioelectron.* **2022**, *210*, 114319. https://doi.org/10.1016/j.bios.2022.114319.
6. Wang, Z.; Zhu, L.; Wang, J.; Zhuang, R.; mu, p.; Wang, J.; Yan, W. Advances in functional guest materials for resistive gas sensors. *RCS Adv.* **2022**, *12*, 24614. https://doi.org/10.1039/d2ra04063h.
7. Yang, B.; Myung, N.V.; Tran, T.T. 1D metal oxide semiconductor materials for chemiresistive gas sensors: A review. *Adv. Electron. Mater.* **2021**, *7*, 2100271. https://doi.org/10.1002/aelm.202100271.
8. Kaur, N.; Singh, M.; Comini, E. One-dimensional nanostructured oxide chemoresistive sensors. *Langmuir* **2020**, *36*, 6326–6344. https://doi.org/10.1021/acs.langmuir.0c00701.
9. Dharmalingam, G.; Sivasubramaniam, R.; Parthiban, S. Quantification of ethanol by metal-oxide-based resistive sensors: A review. *J. Electron. Mater.* **2020**, *49*, 5, 3009–3024. https://doi.org/10.1007/s11664-020-08039-4.

10. Thu, D.T.; Liu, Z.H.; Lee, Y.C.; Kuo, T.W.; Sung, W.L.; Chu, Y.C.; Chuen, Y.L.; Fang, W. A miniaturized CMOS-MEMS amperometric gas sensor for rapid ethanol detection. *IEEE Sens. J.* **2023**, *23*, 8, 8128-8137. https://doi.org/10.1109/JSEN.2023.3254881.
11. Baron, R.; Saffell, J. Amperometric gas sensors as a low cost emerging tecnology platform for air quality monitoring applications: A review. *ACS Sens.* **2017**, *2*, 1553–1566. https://doi.org/10.1021/acssensors.7b00620.
12. Zhao, Y.; Wu, G.; Hung, K.M.; Cho, J.; Choi, M.; O Coileain, C.; Duesberg, G.S.; Ren, X.K.; Chang, C.R.; Wu, H.C. Field effect transistor gas sensors based on mechanically exfoliated Van der Waals materials. ACS Appl. *Mater. Interfaces* **2023**, *15*, 17335–17343. https://doi.org/10.1021/acsami.2c23086.
13. Singh, A.K.; Chowdhury, N.K.; Roy, S.C.; Bhowmik, B. Review of thin film transistor gas sensors: Comparison with resistive and capacitive sensors. *J. Electron. Mater.* **2022**, *51*, 1974–2003. https://doi.org/10.1007/s11664-022-09485-y.
14. Zhang, P.; Xiao, Y.; Zhang, J.; Liu, B.; Ma, X.; Wang, Y. Highly sensitive gas sensing platforms based on field effect transistor-A review. *Anal. Chim. Acta* **2021**, *1172*, 338575. https://doi.org/10.1016/j.aca.2021.338575.
15. Zhai, Z.; Zhang, X.; Hao, X.; Niu, B.; Li, C. Metal-organic frameworks materials for capacitive gas sensors. *Adv. Mater. Technol.* **2021**, *6*, 2100127. https://doi.org/10.1002/admt.202100127.
16. McGinn, C.K.; Lamport, Z.A.; Kymissis, I. Review of gravimetric sensing of volatile organic compounds. *ACS Sens.* **2020**, *5*, 1514–1534. https://doi.org/10.1021/acssensors.0c00333.
17. Gardner, E.L.W.; Gardner, J.W.; Udrea, F. Micromachined thermal gas sensors—A review. *Sensors* **2023**, *23*, 681. https://doi.org/10.3390/s23020681.
18. Hossain, M.S.; Hossen, R.; Walid, M.A.A.; Alvi, S.T.; Al-Amin, M.; Sen, S.; Azad, M.M. Design of quasi-shaped spectroscopy based optical sensor for the detection of alcohol. *Sens. Bio-Sens. Res.* **2023**, *41*, 100527. https://doi.org/10.1016/j.sbsr.2023.100572.
19. Zhan, K.; Qin, P.; Jiang, Y.; Chen, Y.; Heinke, L. Optical sensor array of metal-organic-framework-based inverse opal films for the detection and identification of various alcohols. *Sens. Actuators B Chem.* **2023**, *393*, 134271. https://doi.org/10.1016/J.snb.2023.134271.
20. Jibon, R.H.; Khodaei, A.; Priya, P.P.; Rashed, A.N.Z.; Ahammad, S.H.; Hossain, M.A. ZEONEW based hollow rectangular core photonic crystal fiber (PCF) sensor design and numerical investigation for alcohol detection of variant classes. *Opt. Quantum. Electron.* **2023**, *55*, 977. https://doi.org/10.1007/s11082-023-05267-w.
21. Shinde, P.V.; Rout, C.S. Magnetic gas sensing: Working principles and recent developments. *Nanoscale Adv.* **2021**, *3*, 1551. https://doi.org/10.1039/d0na00826e.
22. Vidis, M.; Plecenik, T.; Mosko, M.; Tomasec, S.; Roch, T.; Satrapinskyy, L.; Grancic, B.; Plencenik, A. Gasistor: A memristor based gas-triggered switch and gas sensor with memory. *Appl. Phys. Lett.* **2019**, *115*, 093504. https://doi.org/10.1063/1.5099685.
23. Sivaperuman, K.; Thomas, A.; Thangavel, R.; Thirumalaisamy, L.; Palanivel, S.; Pitchaimuthu, S.; Ahsan, N.; Okada, Y. Binary and ternary metal oxide semiconductor thin films for effective gas sensing applications: A comprehensive review and future prospects. *Prog. Mater. Sci.* **2024**, *142*, 101222. https://doi.org/10.1016/j.pmatsci.2023.101222.
24. Xavier, R.; Sivaperuman, K. Review on the of physical vapor deposition on imminent chemiresistive metal oxide gas sensors and their future scope. *Mater. Today Commun.* **2024**, *38*, 107831. https://doi.org/10.1016/j.mtcomm.2023.107831.
25. Wang, J.; Chen, Y.; Zhang, B.; Wang, G.; Shi, F.; Wang, Y.; Zhang, Z. Conductometric sensor of hierarchical Bi2MoxW1-x O6 microcages in sensing three gases NH3, isopropanol and ethanol. *Sens. Actuators B Chem.* **2023**, *392*, 134084. https://doi.org/10.1016/j.snb.2023.134084.
26. Ab Kadir, R.; Li, Z.; Sadek, A.Z.; Rani, R.A.; Zoolfakar, A.S.; Field, M.R.; Ou, J.Z.; Chrimes, A.F.; Kalantar-Zadeh, K. Electrospun granular hollow SnO2 nanofibers hydrogen gas sensors operating at low temperatures. *J. Phys. Chem. C* **2014**, *118*, 3129–3139. https://doi.org/10.1021/jp411552z.
27. Chung, C.K.; Ku, C.A. An effective resistive-type alcohol vapor sensor using one-step facile nanoporous anodic alumina. *Micromachines* **2023**, *14*, 1330. https://doi.org/10.3390/mi14071330.
28. Tiwary, P.; Mahapatra, R.; Chakraborty, A.K. ZnO nanobristles prepared by one-step thermal decomposition of zinc nitrate as ultra-high response ethanol sensor at room temperature. *J. Mater. Sci. Mater. Electron.* **2019**, *30*, 5464–5469. https://doi.org/10.1007/s10854-019-00839-7.
29. Wang, M.; Zhu, Y.; Meng, D.; Wang, K.; Wang, C. A novel room temperature ethanol gas sensor based on 3D hierarchical flower-like TiO2 microstructures. *Mater. Lett.* **2020**, *277*, 128372. https://doi.org/10.1016/j.matlet.2020.128372.
30. . Tian, X.; Cui, X.; Lai, T.; Ren, J.; Yang, Z.; Xiao, M.; Wang, B.; Xiao, X.; Wang, Y. Gas sensors based on TiO_2 nanostructured materials for the detection of hazardous gases: A review. *Nano Mater. Sci.* **2021**, *3*, 390–403. https://doi.org/10.1016/j.nanoms.2021.05.011.
31. Jayababu, N.; Poloju, M.; Shruthi, J.; Reddy, M.V.R. Semi shield driven p-n heterostructures and their role in enhancing the room temperature ethanol gas sensing performance of NiO/SnO_2 nanocomposites. *Ceram. Int.* **2019**, *45*, 15134–15142. https://doi.org/10.1016/j.ceramint.201904.255.
32. Hezarjaribi, S.T.; Nasirian, S. An enhanced fast ethanol sensor based on zinc oxide/nickel oxide nanocomposite in dynamic situations. *J. Inorg. Organomet. Polym. Mater.* **2020**, *30*, 4072–4081. https://doi.org/10.1007/s10904-020-01556-z.
33. Wang, C.; Wang, Z.G.; Xi, R.; Zhang, L.; Zhang, S.H.; Wang, L.J.; Pan, G.B. In situ synthesis of flower-like ZnO on GaN using electrodeposition and its application as ethanol gas sensor at room temperature. *Sens. Actuators B Chem.* **2019**, *292*, 270–276. https://doi.org/10.1016/j.snb.2019.04.140.

34. Jayababu, N.; Poloju, M.; Shruthi, J.; Reddy, M.V.R. NiO decorated CeO_2 nanostructures as room temperature isopropanol gas sensors. *RSC Adv.* **2019**, *9*, 13765–13775. https://doi.org/10.1039/c9ra00441f.
35. Garcia-Osorio, D.; Hidalgo-Falla, P.; Peres, H.E.M.; Goncalves, J.M.; Araki, K.; Garcia-Segura, S.; Picasso, G. Silver hehances hematite nanoparticles based ethanol sensor response and selectivity at room temperature. *Sensors* **2021**, *21*, 440. https://doi.org/10.3390/s21020440.
36. Bhowmik, B.; Dutta, K.; Bhattacharyya, P. An efficiet room temperature ethanol sensor device based on p-n homojunction of TiO_2 nanostructures. *IEEE Trans. Electron. Devices* **2019**, *66*, 1063–1068. https://doi.org/10.1109/TED.2018.2885360.
37. Nascimento, E.P.; Firmino, H.C.T.; Santos, A.M.C.; Sales, H.B.; Silva, V.D.; Macedo, D.A.; Neves, G.A.; Medeiros, E.S.; Menezes, R.R. Facile synthesis of hollow F-doped SnO2 nanofibers and their efficiency in ethanol sensing. *J. Am. Ceram. Soc.* **2021**, *104*, 1297–1308. https://doi.org/10.1111/jace.17580.
38. Wu, L.; Shi, X.; Du, H.; An, Q.; Li, Z.; Xu, H.; Ran, H. Ce-doped $LaCoO_3$ film as a promising gas sensor for ethanol. *AIP Adv.* **2021**, *11*, 055305. https://doi.org/10.1063/5.0049923.
39. Bui, H.; Shin, J.H. Perovskite materials for sensing applications: Recent advances and challenges. *Microchem. J.* **2023**, *191*, 108924. https://doi.org/10.1016/j.microc.20.23.108924.
40. Wang, J.; Chen, R.; Xiang, L.; Komarneni, S. Synthesis, properties and applications of ZnO nanomaterials with oxygen vacancies: A review. *Ceram. Int.* **2018**, *44*, 7357. https://doi.org/10.1016/ceramint.2018.02.013.
41. Al-Hashem, M.; Akbar, S.; Morris, P. Role of oxygen vacancies in nanostructured metal-oxide gas sensors: A review. *Sens. Actuators B Chem.* **2019**, *301*, 126845. https://doi.org/10.1016/J.snb.2019.126845.
42. Ul Abideen, Z.; Choi, J.G.; Yuwono, J.A.; Kiy, A.; Kumar, P.V.; Murugappan, K.; Lee, W.J.; Kluth, P.; Nisbet, D.R.; Tran-Phu, T.; et al. Oxygen vacancies engineering in thick semiconductor films via deep ultraviolet photoactivation for selective and sensitive gas sensing. *Adv. Electron. Mater.* **2023**, *9*, 2200905. https://doi.org/10.1002/aelm.202200905.
43. Tomic, M.; Fohlerova, Z.; Gracia, I.; Figueras, E.; Cane, C.; Vallejos, S. UV-light activated APTES modified WO_{3-x} nanowires sensitive to ethanol and nitrogen dioxide. *Sens. Actuators B Chem.* **2021**, *328*, 129046. https://doi.org/10.1016/j.snb.2020.129046.
44. Paun, C.; Motelica, L.; Ficai, D.; Ficai, A.; Andronescu, E. Metal-organic frameworks: Versatile platforms for biomedical applications. *Materials* **2023**, *16*, 6143. https://doi.org/10.3390/ma16186143.
45. Wang, H.; Pei, X.; Kalmutzki, M.J.; Yang, J.; Yaghi, O.M. Large cages of zeolitic imidazolate frameworks. *Acc. Chem. Res.* **2022**, *55*, 707–721. https://doi.org/10.1021/acs.accounts.1c00740.
46. Bose, R.; Ethiraj, J.; Sridhar, P.; Varghese, J.J.; Kaisare, N.S.; Selvam, P. Adsorption of hydrogen and carbon dioxide in zeolitic imidazolate framework structure with SOD topology: Experimental and modelling studies. *Adsorption* **2020**, *26*, 1027–1038. https://doi.org/10.1007/s10450-020-00219-2.
47. Coudert, F.X. Molecular mechanism of swing effect in zeolitic imidazolate framework ZIF-8: Continuous deformation upon adsorption. *Chem. Phys. Chem.* **2017**, *18*, 2732–2738. https://doi.org/10.1002/cphc.201700463.
48. Quin, Y.; Xie, J.; Liu, S.; Bai, Y. Selective methanol-sensing of SnS-supported ultrathin ZIF-8 nanocomposite with core-shell heterostructure. *Sens. Actuators B Chem.* **2022**, *368*, 132230. https://doi.org/10.1016/j.snb.2022.132230.
49. Qui, Y.; Wang, X.; Zang, J. Ultrasensitive ethanol sensor based on nano-Ag&ZIF-8 co-modified SiNWs with enhanced moisture resistance. *Sens. Actuators B Chem.* **2021**, *340*, 129959. https://doi.org/10.1016/j.snb.2021.129959.
50. Meng, Z.; Stolz, R.M.; Mendecki, L.; Mirica, K.A. Electrically-transduced chemical sensors based on two- dimensional nanomaterials. *Chem. Rev.* **2019**, *119*, 478–598. https://doi.org/10.1021/acs.chemrev.8b00311.
51. Wang, M.; Zhang, Z.; Zhong, H.; Huang, X.; Li, W.; Hambsch, M.; Zhang, P.; Wang, Z.; St. Petkov, P.; Heine, T.; et al. Surface-modified phthalocyanine-based two-dimensional conjugated metal–organic framework films for polarity-selective chemiresistive sensing. *Angew. Chem. Int. Ed.* **2021**, *60*, 18666–18672. https://doi.org/10.1002/anie.202104461.
52. Lim, H.; Kwon, H.; Kang, H.; Jang, J.E.; Kwon, H.J. Laser-induced and MOF-derived metal oxide/carbon composite for synergistically improved ethanol sensing at room temperature. *Nano-Micro Lett.* **2024**, *16*, 113. https://doi.org/10.1007/s40820-024-01332-5.
53. Yao, B.; Cui, X.; Tian, X.; Xing, X.; Chen, T.; Wang, Y. SnO_2 submicron porous cube derived from metal-organic framework for n-butanol sensing at room temperature. *Ceram. Int.* **2023**, *49*, 25477–25485. https://doi.org/10.1016/j.ceramint.2023.05.088.
54. Cui, X.; Tian, X.; Xing, X.; Chen, T.; Wang, Y. Au modified hollow cube Sn-MOF derivatives for highly sensitive, great selective, and stable detection of n-butanol at room temperature. *Adv. Mater. Technol.* **2023**, *8*, 2300572. https://doi.org/10.1002/admt.202300572.
55. Mo, R.; Han, D.; Yang, C.; Tang, J.; Wang, F.; Li, C. MOF-derived porous Fe_2O_3 nanocubes combined with reduced graphene oxide for n-butanol room temperature gas sensing. *Sens. Actuators B Chem.* **2021**, *330*, 129326. https://doi.org/10.1016/j.snb.2020.129326.
56. Schedin, F.; Geim, A.K.; Morozov, S.V.; Hill, E.W.; Blake, P.; Katsnelson, M.I.; Novoselov, K.S. Detection of individual gas molecules adsorbed on graphene. *Nat. Mater.* **2007**, *6*, 652–655. https://doi.org/10.1038/nmat1967.
57. Tiwary, P.; Chatterjee, S.G.; Singha, S.S.; Mahapatra, R.; Chakraborty, A.K. Room temperature ethanol sensing by chemically reduced graphene oxide film. *FlatChem* **2021**, *30*, 100317. https://doi.org/10.1016/j.flatc.2021.100317.
58. Abdollahi, H.; Samkan, M.; Bayat, M. Graphene oxide nanoribbons for ethanol detection at room temperature. *Mater. Res. Express* **2019**, *6*, 075053. https://doi.org/10.1088/2053-1591/aaf0df.
59. Sun, D.; Luo, Y.; Debliquy, M.; Zhang, C. Graphene-enhanced metal oxide gas sensors at room temperature: A review. *Beilstein J. Nanotechnol.* **2018**, *9*, 2832–2844. https://doi.org/10.3762/bjnano.9.264.

60. Pienutsa, N.; Roongruangsree, P.; Seedokbuab, V.; Yannawibut, K.; Phatoomvijitwong, C.; Srinives, S. SnO_2-graphene composite gas sensor for a room temperature detection of ethanol. *Nanotechnology* **2021**, *32*, 115502. https://doi.org/10.1088/1361-6528/abcfea.
61. Kaur, N.; Singh, M.; Casotto, A.; Arachchige, H.M.M.M.; Sangaletti, L.; Comini, E. Quenching of oxygen-related defects in graphene oxide nanohybrid: Highly selective room-temperature ethanol sensor. *Appl. Phys. Rev.* **2022**, *9*, 041407. https://doi.org/10.1063/5.0114607.
62. Mehmood, S.; Zhao, X.; Bhopal, M.F.; Khan, F.U.; Yang, Y.; Wang, G.; Pan, X. MoO_2-Ni-graphene ternary nanocomposite for a high- performance room-temperature ethanol gas sensor. *Appl. Surf.Sci.* **2021**, *554*, 149595. https://doi.org/10.1016/j.apsusc.2021.149595.
63. Morsy, M.; Yahia, I.S.; Zahran, H.Y.; Ibrahim, M. Hydrothermal synthesis of CNTs/Co_3O_4@rGO mesoporous nanocomposite as a room temperature gas sensor for VOCs. *J. Inorg. Organomet. Polym. Mater.* **2019**, *29*, 416–422. https://doi.org/10.1007/s10904-018-1011-8.
64. Tung, T.T.; Tran, M.T.; Feller, J.F.; Castro, M.; Ngo, T.V.; Hassan, K.; Nine, M.J.; Losic, D. Graphene and metal organic frameworks (MOFs) hybridization for tunable chemoresistive sensors for detection of volatile organic compounds (VOCs) biomarkers. *Carbon* **2020**, *159*, 333–344. https://doi.org/10.1016/j.carbon.2019.12.010.
65. Hassan, K.; Tung, T.T.; Yap, P.L.; Rastin, H.; Stanley, N.; Nine, M.J.; Losic, D. Fractal design for advancing the performance of chemoresistive sensors. *ACS Sens.* **2021**, *6*, 3685–3695. https://doi.org/10.1021/acssensors.1c01449.
66. Lu, T.; Al-Hamry, A.; Rosolen, J.M.; Hu, Z.; Hao, J.; Wang, Y.; Adiraju, A.; Yu, T.; Matsubara, E.Y.; Kanoun, O. Flexible impedimetric electronic nose for high-accurate determination of individual volatile organic compounds bytuning the graphene sensitive properties. *Chemosensors* **2021**, *9*, 360. https://doi.org/10.3390/chemosensors9120360.
67. Basharnavaz, H.; Habibi-Yangjeh, A.; Pirhashemi, M. Graphitic carbon nitride as a fascinating adsorbent for toxic gases: A mini-review. *Chem. Phys. Lett.* **2020**, *754*, 137676. https://doi.org/10.1016/j.cplett.2020.137676.
68. Dong, Y.; Wang, Q.; Wu, H.; Chen, Y.; Lu, C.H.; Chi, Y.; Yang, H.H. Graphitic carbon nitride materials: Sensing, imaging anf therapy. *Small* **2016**, *12*, 5376–5393. https://doi.org/10.1002/smll.201602056.
69. Sahani, S.; Park, S.J.; Myung, Y.; Pham, T.H.; Tung, T.T.; Kim, T.Y. Enhanced room-temperature ethanol detection by quasi 2D nanosheets of an exfoliated polymeric graphitized carbon nitride composite-based patterned sensor. *ACS Omrga* **2022**, *7*, 41905–41914. https://doi.org/10.1021/acsomega.2c02962.
70. Qiu, J.; Hu, X.; Shi, L.; Fan, J.; MJin, X.; Zhang, W.; Wang, J. Enabling selective, room-temperature gas detection using atomically dispersed Zn. *Sens. Actuators B Chem.* **2021**, *392*, 129221. https://doi.org/10.1016/J.snb.2020.129221.
71. Gu, F.; Luo, C.; Han, D.; Hong, S.; Wang, Z. Atomically dispersed Pt on 3DOM WO_3 promoted with cobalt and nickel oxides for highly selective and highly sensitive detection of xylene. *Sens. Actuator B Chem.* **2019**, *297*, 126772–126782. https://doi.org/10.1016/j.snb.2019.126772.
72. Gu, F.; Cui, Y.; Han, D.; Hong, S.; Flytzani-Stephanopoulos, M.; Wang, Z. Atomically dispersed Pt (II) on WO_3 for highly selective sensing and catalytic oxidation of triethylamine. *Appl. Catal. B Environ.* **2019**, *256*, 117809–117818. https://doi.org/10.1016/j.apcatb.2019.117809.
73. David, S.P.S.; Veeralakshmi, S.; Priya, M.S.; Nehru, S.; Kalaiselvam, S. Room-temperature chemiresistive g-C_3N_4/Ag_2ZrO_3 nanocomposite gas sensor for ethanol detection. *J. Mater. Sci. Mater. Electron.* **2022**, *33*, 11498–11510. https://doi.org/10.1007/s10854-022-08124-w.
74. Chhowalla, M.; Liu, Z.; Zhang, H. Two-dimensional transition metal dichalcogenide (TMD) nanosheets. *Chem. Soc. Rev.* **2015**, *44*, 2584–2586. https://doi.org/10.1039/c5cs90037a.
75. Zhang, D.; Cao, Y.; Wu, J.; Zhang, X. Tungsten trioxide nanoparticles decorated tungsten disulfide nanoheterojunction for highly sensitive ethanol gas sensing application. *Appl. Surf. Sci.* **2020**, *503*, 144063. https://doi.org/10.1016/j.apsusc.2019.144063.
76. Tian, X.; Wang, S.; Li, H.; Li, M.; Chen, T.; Xiao, X.; Wang, Y. Recent advances in MoS2-based nanomaterial sensors for room-temperature gas detection: A review. *Sens. Diagn.* **2023**, *2*, 361. https://doi.org/10.1039/d2sd00208f.
77. Halvaee, P.; Dehghani, S.; Mohammadzadeh, M. Room temperature methanol sensors based on rod-shaped nanostructures of MoS2 functionalized with Ag nanoparticles. *IEEE Sens. J.* **2021**, *21*, 4233–4240. https://doi.org/10.1109/JSEN.2020.3035753.
78. Zhang, J.; Li, T.; Guo, J.; Hu, Y.; Zhang, D. Two-step hydrothermal fabrication of CeO_2-loaded MoS_2 nanoflowers for ethanol gas sensing application. *Appl. Surf. Sci.* **2021**, *568*, 150942. https://doi.org/10.1016/j.apsusc.2021.150942.
79. Das, S.; Sharma, S.; Sharma, S.K. Fa Facile synthesis of 2D-HfS2 flakes for μ-IDE-based methanol sensor: Fast detection at room temperature. *IEEE Sens. J.* **2019**, *19*, 9090–9096. https://doi.org/10.1109/JSEN.2019.2925027.
80. Rana, C.; Bera, S.R.; Saha, S. Growth of SnS nanoparticles and its ability as ethanol gas sensor. *J. Mater. Sci. Mater. Electron.* **2019**, *30*, 2016−2029. https://doi.org/10.1007/s10854-018-0473-3.
81. Shan, W.; Fu, Z.; Ma, M.; Liu, Z.; Xue, Z.; Xu, J.; Zhang, F.; Li, Y. Facile chemical bath synthesis of SnS nanosheets and their ethanol sensing properties. *Sensors* **2019**, *19*, 2581. https://doi.org/10.3390/s191125581.
82. Qin, Y.; Bai, Y.; Xie, J.; Gui, H. Novel insights into the unique intrinsic sensing essences of 2D tin chalcogenides for ethanol: From hexagonal SnS_2 to orthorhombic SnS. *Vacuum* **2023**, *207*, 111616. https://doi.org/10.1016/j.vacuum.2022.111616.
83. Qin, Y.; Chen, S.; Bai, Y. Adsorption and sensing performance toward methanol vapor on SnS/SnS_2 in-plane heterostructures. ACS Appl. *Electron. Mater.* **2022**, *4*, 158–167. https://doi.org/10.1021/acsaelm.1c00911.
84. Qin, Y.; Wang, J.; Bai, Y. Graphene-oriented construction of 2D SnS for methanol gas-sensor application. *Phys. Status Solidi A* **2021**, *218*, 2000642. https://doi.org/10.1002/pssa.202000642.
85. Qin, Y.; Bai, C.; Qiu, P. Alkalized SnS nanoflakes with enhanced sensing properties towards methanol vapor. *ECS J. Solid State Sci. Technol.* **2020**, *9*, 121013. https://doi.org/10.1149/2162-8777/abd51a.

86. Bu, W.; Zhang, Y.; Qiu, Q.; Li, Y.; Zhou, Z.; Hu, C.; Chuai, X.; Wang, T.; Sun, P.; Lu, G. Homojunction between cubic/hexagonal CdS nanocrystal for high and fast response to n-propanol. *Sens. Actuator B Chem.* **2022**, *369*, 132281. https://doi.org/10.1016/j.snb.2022.132281.
87. Qin, Y.; Liang, Y.; Zhou, C.; Bai, Y. Homogeneous heterophase junction based on cubic/orthomorphic SnS for chemiresistive room temperature trace-ethanol sensor. *Sens. Actuator B Chem.* **2024**, *404*, 135285. https://doi.org/10.1016/j.snb.2024.135285.
88. Qiu, P.; Qin, Y.; Bai, Y. Ultra-sensitive methanol detection based on S-vacancy enriched SnS: A combined theoretical and experimental investigation. *Vacuum* **2022**, *198*, 110880. https://doi.org/10.1016/j.vacuum.2022.110880.
89. Qin, Y.; Qiu, P.; Bai, Y. First-principles calculations combined with experiments to study the gas-sensing performance of Zn-substituted SnS. *Phys. Chem. Chem. Phys.* **2020**, *22*, 17513–17522. https://doi.org/10.1039/d0cp01521k.
90. Qin, Y.; Wang, X. Experiments combined with first-principles calculations to compare the enhancement of Ag-doping and -functionalization on the sensing properties of two-dimensional SnS. *Physica E low Dimens. Syst. Nanostruct.* **2021**, *131*, 114752. https://doi.org/10.1016/j.physe.2021.114752.
91. Kuchi, P.S.; Roshan, H.; Sheikhi, M.H. A novel room temperature ethanol sensor based on PbS:SnS_2 nanocomposite with enhanced ethanol sensing properties. *J. Alloys Compd.* **2020**, *816*, 152666. https://doi.org/10.1016/j.jallcom.2019.152666.
92. Roshan, H.; Kuchi, P.S.; Sheikhi, M.H.; Mirzaei, A. Enhancement of room temperature ethanol sensing behavior of PbS–SnS2 nanocomposite by Au decoration. *Mater. Sci. Semicond. Process* **2021**, *127*, 105742. https://doi.org/10.1016/j.mssp.2021.105742.
93. Naguib, M.; Kurtoglu, M.; Presser, V.; Lu, J.; Niu, J.; Heon, M.; Hultman, L.; Gogotsi, Y.; Barsoum, M.W. Two-dimensional nanocrystals produced by exfoliationof Ti_3AlC_2. Adv. *Mater.* **2011**, *23*, 4248–4253. https://doi.org/10.1002/adma.201102306.
94. Anasori, B.; Lukatskaya, M.R.; Gogotsi, 2D metal carbides and nitrides (MXenes) for energy storage. *Nat. Rev. Mater.* **2017**, *2*, 16098. https://doi.org/10.1038/natrevmats.2016.98.
95. Aghei, S.M.; Aasi, A.; Panchapakesan, B. Experimental and theoretical advances in MXene-based gas sensors. *ACS Omega* **2021**, *6*, 2450–2461. https://doi.org/10.1021/acsomega.0c05766.
96. Tang, R.; Xiong, S.; Gong, D.; Deng, Y.; Wang, Y.; Su, L.; Ding, C.; Yang, L.; Liao, C. Ti_3C_2 2D MXene: Recent progress and perspectives in photocatalysis. *ACS Appl. Mater. Interfaces* **2020**, *12*, 56663–56680. https://doi.org/10.1021/acsami.0c12905.
97. Lee, E.; VahidMohammadi, A.; Prorok, B.C.; Yoon, Y.S.; Beidaghi, M.; Kim, D.-J. Room temperature gas sensing of two-dimensional titanium carbide (MXene). *ACS Appl. Mater. Interfaces* **2017**, *9*, 37184−37190. https://doi.org/10.1021/acsami.7b11055.
98. Shuck, C.E.; Han, M.; Maleski, K.; Hantanasirisakul, K.; Kim, S.J.; Choi, J.; Reil, W.E.; Gogotsi, Y. Effect of Ti_3AlC_2 MAX phase on structure and properties of resultant Ti_3C_2Tx MXene. *ACS Appl. Nano Mater.* **2019**, *2*, 3368−3376. https://doi.org/10.1021/acsanm.9b00286.
99. Koh, H.J.; Kim, S.J.; Maleski, K.; Cho, S.Y.; Kim, Y.J.; Ahn, C.W.; Gogotsi, Y.; Jung, H.T. Enhanced selectivity of MXene gas sensors through metal ion intercalation: In situ X-ray diffraction study. *ACS Sens.* **2019**, *4*, 1365−1372. https://doi.org/10.1021/acssensors.9b00310.
100. Chen, W.Y.; Jiang, X.; Lai, S.N.; Peroulis, D.; Stanciu, L. Nanohybrids of a MXene and transition metal dichalcogenide for selective detection of volatile organic compounds. *Nat. Commun.* **2020**, *11*, 1−10. https://doi.org/10.1038/s41467-020-15092-4.
101. Hou, M.; Gao, J.; Yang, L.; Guo, S.; Hu, T.; Li, Y. Room temperature gas sensing under UV light irradiation for Ti_3C_2Tx MXene derived lamellar TiO_2-C/g-C_3N_4 composites. *App. Surf. Sci.* **2021**, *535*, 147666. https://doi.org/10.1016/j.apsusc.2020.147666.
102. Raghu, A.V.; Karuppanan, K.K.; Nampoothiri, J.; Pullithadathil, B. Wearable, flexible ethanol gas sensor based on TiO_2 nanoparticles-grafted 2D-titanium carbide canosheets. *ACS Appl. Nano Mater.* **2019**, *2*, 1152–1163. https://doi.org/10.1021/acsanm.8b01975.
103. Liu, M.; Wang, Z.; Song, P.; Yang, Z.; Wang, Q. In_2O_3 nanocubes/Ti_3C_2Tx MXene composites for enhanced methanol gas sensing properties at room temperature. *Ceram. Int.* **2021**, *47*, 23028–23037. https://doi.org/10.1016/j.ceramint.2021.05.016.
104. Yao, Y.; Han, Y.; Zhou, M.; Xie, L.; Zhao, X.; Wang, Z.; Barsan, N.; Zhu, Z. MoO_3/TiO_2/Ti_3C_2Tx nanocomposite based gas sensors for highly sensitive and selective isopropanol detection at room temperature. *J. Mater. Chem. A* **2022**, *10*, 8283–8292. https://doi.org/10.1039/d1ta11018g.
105. Zhang, S.; Song, P.; Zheng, Y.; Ding, Y.; Wang, Q. MoO_2/MoO_3/MXene ternary nanocomposites for high-performance ethanol detection at room temperature. *J. Alloys Compd.* **2022**, *925*, 166663. https://doi.org/10.1016/j.jallcom.2022.166663.
106. Nylabder, C.; Armgrath, M.; Lundstrom, I. An ammonia detector based on a conducting polymer. *Anal. Chem. Symp. Ser.* **1983**, *17*, 203–207.
107. Samanta, S.; Roy, P.; Kar, P. Sensing of ethanol and other alcohol contaminated ethanol by conducting functional poly(o-phenylenediamine). *Mater. Sci. Eng. B* **2020**, *256*, 114541. https://doi.org/10.1016/j.mseb.2020.114541.
108. Cobianu, C.; Serban, B.C.; Dumbravescu, N.; Buiu, O.; Avramescu, V.; Pachiu, C.; Bita, B.; Bumbac, M.; Nicolescu, C.M.; Cobianu, C. Organic-inorganic ternary nanohybrids of single-walled carbon nanohorns for room temperature chemiresistive ethanol detection. *Nanomaterials* **2020**, *10*, 2552. https://doi.org/10.3390/nano10122552.
109. Fratoddi, I.; Venditti, I.; Cametti, C.; Russo, M.V. Chemiresistive polyaniline-based gas sensors: A mini review. *Sens. Actuators B Chem.* **2015**, *220*, 534–548. https://doi.org/10.1016/J.snb.2015.05.107.
110. Al-Haidary, Q.N.; Al-Mokaram, A.M.; Hussein, F.M.; Ismail, A.H. Development of polyaniline for sensor applications: A review. *J. Phys. Conf. Ser.* **2021**, *1853*, 012062. https://doi.org/10.1088/1742-6596/1853/1/012062.
111. Pal, R.; Goyal, S.L.; Rawal, I.; Sharma, S. Efficient room temperature methanol sensors based on polyaniline/graphene micro/nanocomposites. *Iran. Polym. J.* **2020**, *29*, 591–603. https://doi.org/10.1007/s13726-020-00822-8.

112. Tan, C.K.; Blackwood, D.J. Interactions between polyaniline and methanol vapour. *Sens. Actuators B Chem.* **2000**, *71*, 184–191. https://doi.org/10.1016/S0925-4005(00)00615-8.
113. Li, Y.; Zheng, Y. Preparation and electrochemical properties of polyaniline/reduced graphene oxide composites. *J. Appl. Polym. Sci.* 2018, 135, 46103. https://doi.org/10.1002/app.46103.
114. Jung, J.W.; Son, S.H.; Choi, J. Polyaniline/reduced graphene oxide composites for hole transporting layer of high-performance inverted perovskite solar cell. *Polymers* **2021**, *13*, 1281. https://doi.org/10.3390/polym13081281.
115. Kumar, M.; Supreet; Sharma, S.; Goyal, S.L.; Kumar, S.; Chauhan, S.; Vidhani, B.; Pal, R. Composite nanoarchitectonics with reduced-graphene oxide and polyaniline for a highly responsive and selective sensing of methanol vapors. *Mater. Chem. Phys.* **2024**, *312*, 128626. https://doi.org/710.1016/j.matchemphys.2023.128626.
116. Kumar, M.; Sharma, S.; Pal, R.; Vidhani, B. Supreet a novel gas sensor based on activated charcoal and polyaniline composites for selective sensing of methanol vapors. *Sens. Actuators A Phys.* **2023**, *353*, 114210. https://doi.org/10.1016/j.sna.2023.114210.
117. Kumar, Y.R.; Deshmukh, K.; Sadasivuni, K.K.; Pasha, S.K.K. Graphene quantum dot based materials for sensing, bio-imaging and energy storage applications: A review. *RSC Adv.* **2020**, *10*, 23861. https://doi.org/10.1039/d0ra03938a.
118. Masemola, C.M.; Moloto, N.; Tetana, Z.N.; Gqoba, S.S.; Mubiayi, P.K.; Linganiso, E.C. N-doped graphene quantum dot-modified polyaniline for room-temperature sensing of alcohol vapors. *Mater. Chem. Phys.* **2022**, *287*, 126229. https://doi.org/10.1016/j.matchemphys.2022.126229.
119. Zhang, Y.; Pan, W.; Dong, G.; Zhang, D. A high-performance room temperature methanol gas sensor based on alpha-iron oxide/polyaniline/PbS quantum dots nanofilm. *J. Mater. Sci. Electron.* **2019**, *30*, 17907–17915. https://doi.org/10.1007/s10854-019-02143-w.
120. Pal, R.; Goyal, S.L.; Rawal, I. Selective methanol sensors based on polyaniline/V_2O_5 nanocomposites. *Iran. Polym. J.* **2022**, *31*, 519–532. https://doi.org/10.1007/s13726-022-01024-0.
121. Zhang, R.; Pang, W.; Feng, Z.; Chen, X.; Chen, Y.; Zhang, Q.; Zhang, H.; Sun, C.; Yang, J.J.; Zhang, D. Enabling selectivity and fast recovery on ZnO nanowire gas sensors through resistive switching. *Sens. Actuators B Chem.* **2017**, *238*, 357–363. https://doi.org/10.1016/J.snb.2016.07.068.
122. Lee, D.; Yun, M.J.; Kim, K.H.; Kim, S.; Kim, H.D. Advanced recovery and high sensitive properties of memristor-based gas sensor devices operated at room temperature. *ACS Sens.* **2021**, *6*, 4217–4224. https://doi.org/10.1021/acssensors.1.c01840.
123. Qiu, P.; Qin, Y.; Xia, Q. Ultrasensitive memristor-based gas sensor (gasistor) with gas-triggered switch and memory function for dilute NH_3 detection. *Sens. Actuators B Chem.* **2022**, *373*, 132730. https://doi.org/10.1016/j.snb.2022.132730.
124. Huang, C.H.; Chou, T.S.; Huang, J.S.; Lin, S.M.; Chueh, Y.L. Self-selecting resisitive swithching scheme using TiO_2 nanorod arrays. *Sci. Rep.* **2017**, *7*, 2066. https://doi.org/10.1038/s41598-017-01354-7.
125. Zhou, Z.; Yang, F.; Wang, S.; Wang, L.; Wang, X.; Wang, C.; Xie, Y.; Liu, Q. Emerging of two-dimensional materials in novel memristor. *Front. Phys.* **2022**, *17*, 2, 23204. https://doi.org/10.1007/s11467-021-1114-5.
126. Pereira, M.E.; Martins, R.; Fortunato, E.; Barquinha, P.; Kiazadeh, A. Recent progress in optoelectronic memristors for neuromorphic and in-memory computation. *Neuromorph. Comput. Eng.* **2023**, *3*, 022002. https://doi.org/10.1088/2634-4386/acd4e2.
127. Qiu, P.; Qin, Y.; Xia, Q. Ultrasensitive gas sensor developed from SnS/TiO2-based memristor for diluite methanol detection at room temperature. *Sens. Actuators B Chem.* **2023**, *392*, 134038. https://doi.org/10.1016/j.snb.2023.134038.
128. Chae, M.; Lee, D.; Kim, H.D. Low-power consumption IGZO memristor-based gas sensor embedded in an internet of things monitoring system for isopropanol alcohol gas. *Micromachines* **2024**, *15*, 77. https://doi.org/10.3390/mi15010077.
129. Lee, D.; Bae, D.; Chae, M.; Kim, H.D. High sensitivity of isopropyl alcohol gas sensor based on memristor device operated at room temperature. *J. Korean Phys. Soc.* **2022**, *80*, 1065–1070. https://doi.org/10.1007/s40042-022-00470-6.